Two-dimensional materials in photonic integrated circuits: recent developments and future perspectives [Invited]

Hua Tan (谭 华)[1,2], Lei Du (杜 磊)[2], Fenghe Yang (杨丰赫)[2*], Wei Chu (储 蔚)[2**], and Yiqiang Zhan (詹义强)[1]

[1] Centre for Micro Nano Systems, School of Information Science and Technology (SIST), Fudan University, Shanghai 200433, China
[2] Zhangjiang Laboratory, Shanghai 201210, China

*Corresponding author: yangfh@zjlab.ac.cn
**Corresponding author: chuwei@zjlab.ac.cn

The heterogeneous integration of photonic integrated circuits (PICs) with a diverse range of optoelectronic materials has emerged as a transformative approach, propelling photonic chips toward larger scales, superior performance, and advanced integration levels. Notably, two-dimensional (2D) materials, such as graphene, transition metal dichalcogenides (TMDCs), black phosphorus (BP), and hexagonal boron nitride (hBN), exhibit remarkable device performance and integration capabilities, offering promising potential for large-scale implementation in PICs. In this paper, we first present a comprehensive review of recent progress, systematically categorizing the integration of photonic circuits with 2D materials based on their types while also emphasizing their unique advantages. Then, we discuss the integration approaches of 2D materials with PICs. We also summarize the technical challenges in the heterogeneous integration of 2D materials in photonics and envision their immense potential for future applications in PICs.

1. Introduction

The growth of the information industry demands higher communication bandwidth while also requiring significant advancements in computing power. Over the past half-century, microelectronics technology has rapidly evolved following Moore's Law, continuously enhancing information communication and computing capabilities. However, the continued use of Moore's Law becomes challenging when entering the sub-10-nm node era. In addition, power consumption and bandwidth have also become notable bottlenecks for microelectronics technology to overcome[1]. Photonics possesses characteristics such as high speed, high bandwidth, low loss, low latency, and parallelism, granting it unparalleled advantages in the future era of massive information exchange. Photonics exhibits significant advantages in massive information processing due to its high speed, high bandwidth, low loss, low latency, and parallelism characteristics[2–4]. Therefore, photonic integrated circuits (PICs) with high-performance photonic devices serve as promising engines for supporting advanced computing and broadband networks.

Silicon photonics has leveraged the mature complementary metal-oxide-semiconductor (CMOS) infrastructure and design ecosystem, satisfying the modern information industry's demand for PICs in terms of cost and integration scale. As a result, silicon photonics has already played a significant role in high-speed data centers and coherent communications, and it is also driving advancements in applications, such as high-performance computing, artificial intelligence (AI), automotive industry, and biomedical sensing[5]. It is worth noting that silicon photonics still faces significant challenges. As an indirect bandgap material, it is difficult to achieve laser and semiconductor optical amplifiers (SOAs) based on silicon[6]. Furthermore, modulators in silicon photonics, which rely on carrier injection effects, have limitations in the modulation bandwidth[7]. The detectors in silicon photonics are currently implemented by introducing germanium (Ge) in foundries, but the device performance is not optimal[8,9]. Additionally, as the applications diversify and the integration scale expands, silicon photonics also encounter propagation loss and power handling issues.

To address these challenges, a widely recognized approach is the heterogeneous integration of various optoelectronic materials with silicon photonics, allowing each material to leverage its unique advantages and to realize a high-performance PIC. By heterogeneously integrating III–V materials with silicon photonics, it is possible to achieve optical transceivers with on-chip light sources, which are already employed in data centers in the industry[10–12]. Due to its exceptional modulation performance, thin-film lithium niobate (TFLN) material has been successfully integrated into silicon photonics[13–16]. Heterogeneous

integration of silicon photonics with other materials, such as barium titanate (BTO)[17,18], electro-optic polymers[19,20], two-dimensional (2D) materials[21,22], and magneto-optic thin films[23], has also been demonstrated to realize light sources, modulators, detectors, and isolators in PICs. Among these, 2D materials with novel properties have emerged as a viable alternative to facilitate extraordinary progress in improving photonic devices with a smaller footprint and higher performance[24].

Since the first finding of graphene in 2004[25], 2D materials have attracted tremendous attention on integrated photonics. Booming research on 2D materials, such as graphene, transition metal dichalcogenides (TMDCs)[26], black phosphorus (BP)[27] and hexagonal boron nitride (hBN)[28], has been published during the last decades. Compared with traditional bulk materials for integrated photonics, 2D materials exhibit extraordinary properties, including broadband absorption, ultrafast carrier mobility, and strong nonlinear effects, which benefit from their unique optical, electronic, thermal, and mechanical features[22,29,30]. Graphene is a gapless semi-metallic material with a carrier mobility of up to $\sim 2 \times 10^5$ cm^2 V^{-1} s^{-1}, 100 times higher than silicon (Si)[31]. The ultrafast electron transition can fulfill the request of high-speed modulation and detection. Although the zero-bandgap characteristic makes graphene an alternative candidate for broad bandwidth device, it limits the realization of an efficient graphene-based laser. In contrast, monolayer TMDCs are direct-bandgap semiconductors with an $\sim$1.0–2.5 eV bandgap[32,33]. BP is also a kind of direct bandgap of around $\sim$0.3–2 eV from bulk form to monolayer, covering a wide spectral range from the visible to the infrared[34,35]. These emerge as encouraging light-emitting and photodetecting properties, owing to the direct bandgap and quantum confinement in the direction perpendicular to the 2D plane. In addition to graphene, TMDCs, and BP, 2D hBN, an isomorph of graphene with a very similar layered structure, is another promising functional material. Although by itself it is an insulator, hBN can be integrated with other 2D materials by tuning their carrier mobility and protecting them from contamination, oxidation, and thermally/electrically induced degradation[28,36]. Thus, 2D materials exhibit broad applications in optoelectronic devices and could probably pave the way for future PICs desiring higher capability and higher integration.

Despite the fact that 2D materials have demonstrated outstanding characteristics, there are still some problems that need to be addressed before large-scale application. First, the Si-based CMOS compatible fabrication process of the 2D material is one of the key challenges. High quality single-layer or multi-layer 2D materials can be easily obtained by micromechanical exfoliation. But this method of following a transferring process cannot be compatible with a Si-based or a silicon-on-insulator (SOI)-based platform. So far, chemical vapor deposition (CVD) is the most widely used approach for synthesizing large-scale growth with precise control of layer numbers and morphology[37–39]. To obtain high quality materials directly on Si or on SOI, the precursor, the deposition window, and the substrate preparation need to be rigorously investigated, as well as methods that include thermal CVD[40–42], plasma enhanced CVD

(PECVD)[43,44], atomic layer deposition (ALD)[45,46], and metal organic CVD (MOCVD)[47]. Second, because of the 2D nature, the surface status is much active and sensitive to atmosphere and interface. That means 2D material is easy to be oxidized and induce absorption or doping, which will affect the bandgap or downgrade the carrier mobility, and further impact the device performance.

In this review, the advantages and applications of the four state-of-the-art 2D materials, including graphene, TMDCs, BP, and hBN, on photonics devices are systematically discussed in the first three sections. In detail, we summarize and analyze their individual electronic and optical properties and determine which are better available for device construction. In the next section, we introduce recent progress and challenges, as well as the opportunities of using Si-based and SOI-based heterogeneous integration of 2D material. Finally, the last section concludes with the future challenges and perspectives on the development of photonic integration based on 2D materials.

2. Graphene-Integrated PICs

2.1. Optoelectronic basics of graphene

Graphene quickly gained prominence following its discovery in 2004 and has since consistently attracted significant attention in the field of photonic devices and PICs, due to its exceptional optoelectronic properties[48–50]. Graphene is a single carbon atomic layer with a hexagonal honeycomb lattice [Fig. 1(a)], in which π (valence band) and π^* (conduction band) states are noninteracting and form into the Dirac cone-shaped band structure of graphene [Figs. 1(b) and 1(c)][51]. The Fermi level (E_f) in this band structure can be tuned by electrical or chemical methods, which means the optoelectronic properties of graphene can be conveniently tailored for extensive applications[52–54]. Additionally, graphene exhibits ultrafast carrier transports with a carrier mobility as high as $\sim 2 \times 10^5$ cm^2 V^{-1} s^{-1} [55]. The fast electronic transmission in carbon lattices guarantees the requirements of high speed and high bandwidth optoelectronic devices in PICs. These lay theoretical fundamentals for graphene-integrated modulators and detectors. Moreover, the tunable E_f also affects the mechanism of the carrier transitions in the graphene band structures under optical excitation. The interband optical stimulated transition is dominant when the E_f is at the central Dirac point, leading to the maximization of light absorption for graphene [corresponding to minimum transmission in Fig. 1(d)][56]. In the meantime, the gapless bandgap structure enables graphene in the ultrabroad light absorption spectrum ranging from the visible (VIS) to the terahertz (THz) [Fig. 1(f)][57,58], making graphene an auspicious material candidate for use in broadband photodetections.

2.2. Graphene-integrated modulators

Typically, electrical signals are converted into optical signals via integrated modulators, enabling the loading of information onto
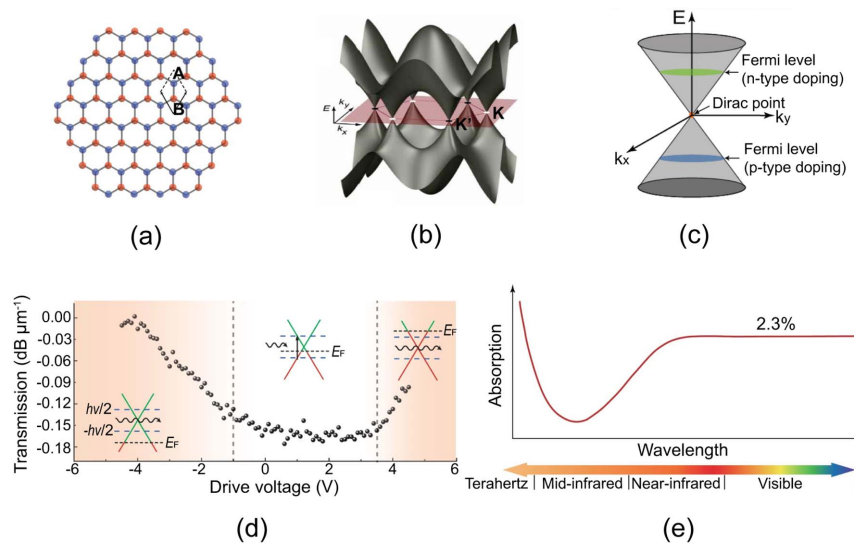
Fig. 1. (a) Hexagonal honenycomb lattice of graphene with two atoms (A and B) per unit cell. (b) 3D band structure of graphene. (c) Approximation of the low energy band structure as two cones touching at the Dirac point. (a)–(c) Reproduced with permission[51]. (d) Transmission of a graphene modulator at different drive voltages and E_f. Reproduced with permission[56]. (e) Graphene absorption as a function of the wavelength. Reproduced with permission[58].

the PICs. The optical signals are encoded in the form of amplitude, phase, polarization, etc. Based on the working principles, modulators can be classified into electro-optical (EO), thermal-optical (TO), and all-optical (AO) categories, among which EO modulators can be further divided into electro-absorption (EA) and electro-refractive (ER) modulators. For modulator devices integrated in PICs, key attributes include modulation bandwidth, modulation depth, insertion loss, power consumption, modulation linearity, and so on. These factors collectively determine the performance of the modulator.

Benefiting from the atomic layer thickness and the large thermal conductivity, graphene can be fabricated into efficient nanoheaters for TO modulators, which have been intensively employed in Si-based PICs[59–62]. The working mechanism of TO modulators relies on the change in the refractive index of the Si materials with the temperature variation induced by the modification of phases and amplitudes in the light propagation. As early as 2014, Yu et al. investigated the graphene-integrated TO modulators.[59,60]. As illustrated in Figs. 1(a) and 1(b), two typical Si photonic structures, Mach−Zehnder interferometers (MZIs) and microdisks, were proposed to integrate with CVD-grown graphene via the fabrication processes of wet-transferring and patterning for the graphene, respectively. In their devices, graphene conducts heat from traditional metal heaters to Si-waveguides with a high thermal efficiency of up to 8.20 K μm³ mW⁻¹ as well as a response time in the range of tens of μs.

Using monolayer graphene nanoheaters instead of traditional metal heaters in PICs has prominent benefits. First, the thermal conductivity of graphene is around 4840 W mK⁻¹ to 5300 W mK⁻¹ [63], which is one order of magnitude higher than that of representative copper (Cu). Second, graphene is almost optically transparent. Negligible excess loss (< 0.0002 dB/μm in

Yu's work) can be obtained when the optimized graphene makes contact with the Si-waveguides without the complex cladding layer design, which is essential for metal heaters to avoid serious metal absorption loss and the decelerating thermal diffusion speed. Moreover, the flexible characteristics of graphene enable it to be hybrid with a series of photonic structures for TO modulators, including waveguide MZIs[59], cavities[61], and resonators[60].

Another special kind of modulators is optical switches, whose superiority is its large modulation depth. More recently, Nakamura et al. showed their work of placing graphene local heaters on racetrack resonators to fabricate the first graphene-integrated TO optical switch [Fig. 2(c)][62]. The device exhibited a high wavelength tuning efficiency of 0.24 nm/mW and a high heating efficiency of 7.66 K μm³ mW⁻¹. In addition, a high-speed modulator at 100 kHz with a rise and fall response time of 1.2 μs and 3.6 μs, respectively, was also achieved on this device [Fig. 2(d)]. In contrast to the response time of a typical metal heater resonator (∼100 μs), graphene nanoheaters display enormous advantages in high thermal modulation efficiency originating from its atomic thermal conductive thickness and large thermal conductivity.

Furthermore, graphene, with its high thermal-optical efficiency, is ideally suited for emerging non-volatile switches or modulators[60,62,64]. These devices typically operate with ultralow programming energy consumption and can serve as fundamental building blocks for neuromorphic computing. In 2022, Fang et al. demonstrated a non-volatile electrically reconfigurable Si-based photonic platform [Figs. 2(e) and 2(f)], leveraging a monolayer graphene heater with high energy efficiency and endurance[64]. The graphene-assisted photonic switches exhibited an endurance of over 1000 cycles and a programming energy density of 8.7 ± 1.4 aJ nm⁻³. It is graphene that promises
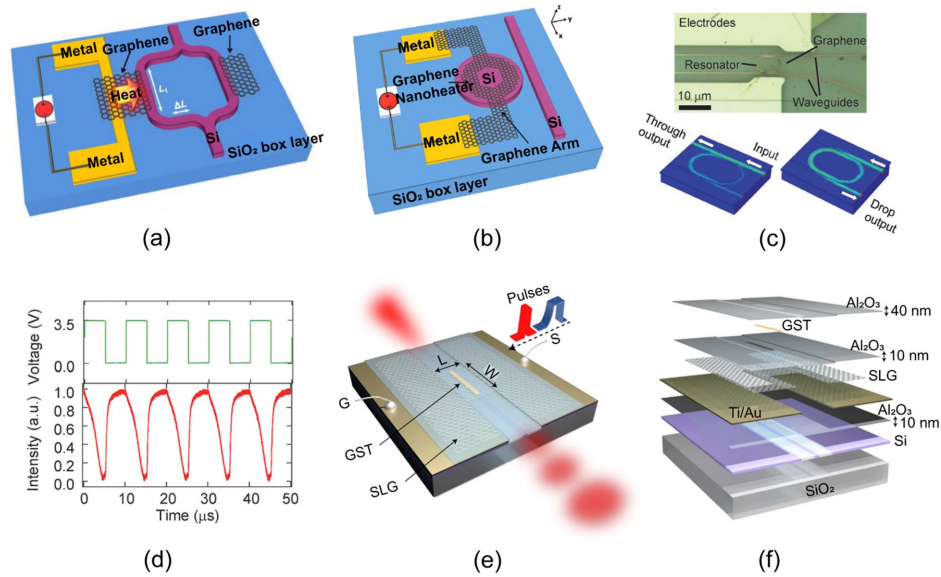
Fig. 2. (a) Schematic of a graphene TO modulator integrated in a Si MZI. Reproduced with permission[59]. (b) Schematic of a graphene TO modulator integrated in a Si microdisk. Reproduced with permission[60]. (c) Schematic and optical microscope images of the resonant optical switch device integrated with a graphene nanoheater. (d) Normalized output intensity from the through port to the graphene. (c) and (d) Reproduced with permission[62]. (e) Schematic and (f) layered structure of a graphene-phase-change material reconfigurable silicon photonic device structure. (e) and (f) Reproduced with permission[64].

at least a twenty-fold reduction in switching energy consumption compared with traditional ones.

Although graphene offers an ultrashort and efficient thermal conductive path, the operation speed of graphene-integrated TO modulators is still limited by the relative slow heat dissipation, with a relaxation time in the order of the magnitude of ms to μs, corresponding to the device modulation bandwidth ranging from kHz to MHz. It encourages us to explore the possibility of using the exceptional optoelectronic properties of graphene, such as its tunable E_f and ultrafast carrier mobility, in an alternative approach to EO modulators in order to improve the modulation speed. As aforementioned, the E_f of graphene significantly impacts its optical absorption and consequently influences the light–matter interactions in PICs. It is also well known that the E_f of semiconductors can be adjusted in different charge states (charge carriers accumulate or deplete) in the classical metal-oxide-semiconductor (MOS) models by controlling the gating voltage. Inspired by that, the graphene-oxide-Si waveguide (GOS) capacitor structure is commonly constructed in graphene-integrated EA modulators for tuning the E_f of graphene and therefore modulating the light absorption in devices. In 2011, Liu *et al.* reported the first graphene Si-based EA modulator by means of the single-layer GOS structure (SLG)[56]. As shown in Fig. 3(a), graphene, dielectric aluminum oxide (Al_2O_3), and Si-waveguide form into a local capacitor, while graphene and the doped Si-waveguide are connected to side electrodes separately. Under ambient conditions, the working spectrum covers a broadband from 1.35 μm to 1.6 μm, and the bandwidth reaches 1 GHz at that time [Fig. 3(b)]. Subsequently, several improvements have been made, aiming at a higher modulation bandwidth[65–70]. For example, by optimizing both

the graphene and Si-waveguide doping to reduce the contact resistance and resistance-capacitance (RC) hysteresis in the circuits, the highest EA bandwidth beyond 15 GHz in a 25-μm-length SLG modulator was experimentally demonstrated [Fig. 3(c)][67]. However, the Si doping methods will also have side effects on the photonic devices such as the ion implant-induced excess optical loss and the degraded modulation depth. To eliminate these issues, the concept of double-layer GOS (DLG) structure was raised by exploiting the semi-metallic property of graphene[71,72]. As shown in Fig. 3(d), the prototype of the GOS structure comprises two coupled graphene nanosheets separated by a dielectric layer, in which the top layer of graphene serves as the gate electrode, whereas the underearth graphene connected with the waveguides, is being charged for absorption modulation[71]. Despite the fact that the proof-of-concept is only operated at 1 GHz, the DLG model achieved continuous development on diverse platforms, such as SOI[73], Si_3N_4[74,75], and polymer-waveguides[76,77], because of its easy processing, reduced capacitive RC constant, and resultant higher modulation speed[72,74,78-80]. Among these, the highest bandwidth of 35 GHz in Si-based PICs, 30 GHz in Si_3N_4-based PICs, and 42 GHz in polymer-waveguide PICs were achieved[74,80].

Graphene-integrated EA modulators exhibit superior modulation bandwidth. However, the intrinsic low absorption of graphene (2.3%) constrains their EA modulation depth[24,81], which is crucial for the performance of the modulators. Moreover, EA modulators often involve a trade-off between operational speed and modulation depth. This occurs because a thicker dielectric layer can reduce RC delays in the GOS structures, but it also results in a diminished gating effect and, consequently, a weaker

modulation depth. Several strategies have been employed to mitigate this trade-off. For instance, microring resonance structures incorporated with graphene have been realized to acquire the high modulation depth ($> 10\,dB$) as well as maintaining the large bandwidth [Fig. 3(e)][75,82,83]. This is because the light transmission in a ring resonance is susceptible to the optical loss induced by the graphene absorption. Other approaches to enhance the graphene-light interaction directly by capturing light within graphene and a photonic-crystal waveguide (PhCW) via slow-light effects[69,73] and using surface plasmons to amplify light absorption at the graphene/dielectric interface[84–86] have been put forward.

Surface plasmons are important physical behavior that represents free electrons in metal/semi-metal oscillating with external electromagnetic fields and result in intense light–matter interactions, which have been widely studied in optoelectronic devices in the past years[87–90]. Graphene itself, is an active plasmonic material, supporting graphene surface plasmons (GSPs) with longer propagation lengths due to a low electron scattering rate[91]. In 2022, Liu *et al.* proposed a dual-layer graphene-assisted EA modulator with orthogonal T-shaped metal slot hybrid plasmonic waveguides [Fig. 3(f)][85], allowing a 3 dB bandwidth of ~127 GHz at the waveguide length of 20 µm, a modulation depth of ~0.5 dB/µm as well as the power consumption of 72 fJ/bit. In addition to the innovation in the waveguide

shapes, some other intriguing plasmonic structures, such as pattern graphene[92] and suspended graphene[93], have also been investigated in EA modulators to boost the device performance.

The tunable E_f of the graphene in the GOS structures can be capable of exhibiting either EA or ER effects when it is incorporated with waveguides. Based on this, ER modulators enabled by the integration of GOS and MZI structures were proposed and evolved rapidly with the benefits of quadrature amplitude modulation (QAM), which can be implemented in long-haul optical communication[94–98]. Among them an optimized graphene-integrated MZI configuration with the maximum extinction ratio of 35 dB, a bandwidth of 5 GHz, and a modulation efficiency of 0.28 V cm at 1550 nm [Figs. 4(a)–4(c)] has been accomplished[96].

The last modulators to be reviewed are the AO types, whose inputs and outputs are all in the optical domain, which might be promising for ultrafast operations at ultralow energy consumptions[99–106]. The working mechanism of AO modulators is based on the variety of graphene extinction coefficients induced by photogenerated carriers in coupled semiconductor-waveguides. In 2019, Ono *et al.* proposed using graphene-loaded deep-subwavelength plasmonic waveguides [Figs. 4(d) and 4(c)] to fabricate the ultrafast AO switch with a switching energy of 35 fJ and a switching time of 260 fs[104]. The ultralow graphene saturation energy of 12 fJ [Fig. 4(e)], realized by the small
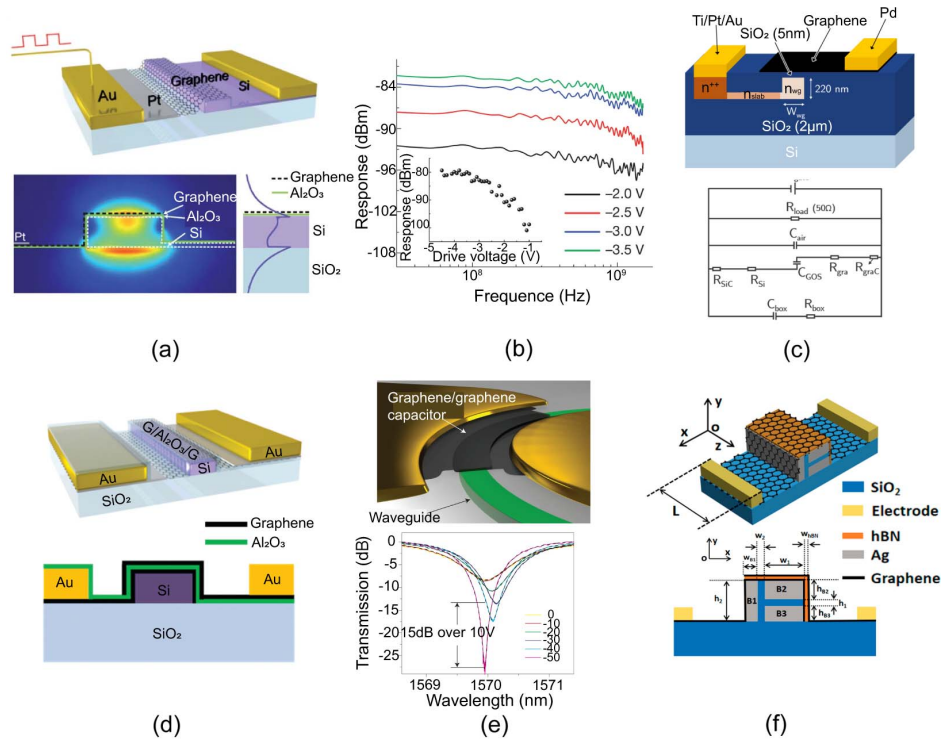
Fig. 3. (a) Schematic and (b) dynamic EO response of the graphene-integrated optical waveguide modulator. (a) and (b) Reproduced with permission[56]. (c) Top: cross-sectional schematic of the SLG EA modulator. Bottom: equivalent electrical circuit of the device. Reproduced with permission[67]. (d) Schematic of the DLG modulator. Top: perspective view. Bottom: cross-sectional view. Reproduced with permission[71]. (e) Schematic (top) and transmission spectra (bottom) of the graphene-integrated ring resonator modulator. Reproduced with permission[74]. (f) 3D (top) and 2D cross-sectional (bottom) schematic of graphene modulator based on metal slot waveguide. Reproduced with permission[85].
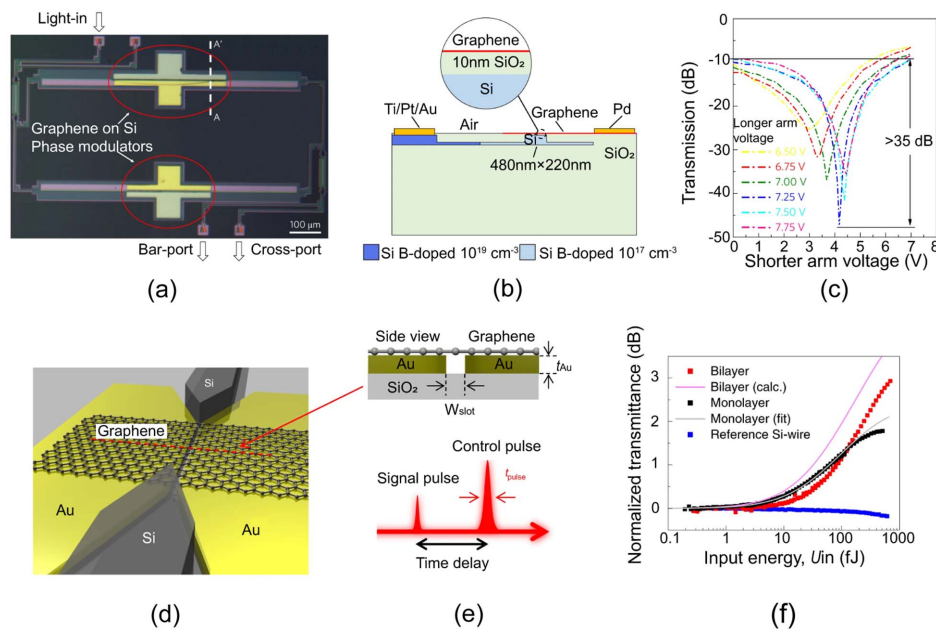
Fig. 4. (a) Optical micrograph, (b) cross section through the dashed line A–A′, and (c) extinction ratio of the graphene-integrated MZI modulator. (a)–(c) Reproduced with permission[96]. (d) Schematic of the graphene-plasmonic slot waveguide AO modulator and (e) the pump probe measurement. (f) Saturable absorption with picosecond laser pulses in the graphene-loaded (monolayer, bilayer) MIM-WGs and the reference Si-wire WG (without graphene). (d)–(f) Reproduced with permission[104].

volume light propagation mode and the local field enhancement in graphene, is the decision factor to extraordinary switching performances in this work. Although AO modulators show remarkable potential in ultralow power and highspeed PICs, their large insertion loss, caused by metal absorption, should not be ignored in applications.

2.3. Graphene-integrated photodetectors

Photodetectors are essential components of PICs. Different from free-space photodetectors working individually for the applications of sensing, detecting, and imaging[89,107-109], photodetectors in PICs are mostly integrated with waveguides in cooperation with other on-chip phonic devices for the realization of PIC functionalities such as optical communication and computing. There are several advantages in waveguide-integrated photodetectors. For example, they have high light confinement in the waveguides for saving footprints, a low signal-to-noise ratio (SNR) due to small detection volumes, and, last but not the least, the opportunity to realize wavelength division multiplexing (WDM) in PICs enabled by broadband modulation and detection within one structure[78]. Photodetectors can be sorted into photovoltaic (PV), photoconductive (PC), photogating (PG), photothermoelectric (PTE), and photobolometric (PBE) types based on their operation principles.

PV photodetectors depend on the built-in electrical potential in the p-n/p-i-n/Schottky junctions to separate photogenerated carriers and drive them to the opposite direction to be collected by electrodes. They can operate under zero bias and also feature the metrics of high speed, low dark current, and low noise. PC

photodetectors leverage the variation in semiconductor conductivity induced by excess free photogenerated carriers to generate photocurrents. These excess free carriers come from their unbalanced lifetime. Usually, the mobility (lifetime) of holes is larger than that of the electrons, resulting in electron accumulation/photoconductive gain in semiconductors at an external voltage. PG effects can be regarded as a special case of PC. The un-bonding surface or defects introduce trap states in the band structure of the semiconductors, and trapped carriers will have a longer lifetime and thus give rise to a higher photocurrent gain. As an expense, the response time and speed of the PC and the PG photodetectors are limited in an order of ms and s.

PTE and PBE photodetectors are associated with thermal effects. PTE effect is also called the Seebeck effect. The Seebeck coefficient might be different within the doping and thickness variance in semiconductors, leading to a temperature gradient ΔT under light illuminations and thereby a carrier-orientated movement-caused voltage V_{PTE} (also called photo-thermoelectric voltage). PTE photodetectors can work without a bias. The PBE effect refers to the semiconductors' resistance change when they are heated by light illuminations. PBE photodetectors are superior in ultrabroad optical responses, ranging from middle-infrared (MIR) to far-infrared (FIR). The key characteristic parameters of photodetectors contain a response spectrum, quantum efficiency, photoresponsivity, response speed, and noise equivalent power (NEP). In the following review, we will start with the graphene properties and subsequently explain the role that graphene plays in different types of photodetectors.

With its unmatched properties in photodetection, such as broad-spectrum absorption, ultrafast responses, and strong

electron–electron interactions, graphene was the pioneering 2D material employed in photodetectors as early as 2009[110,111]. However, the intrinsic light absorption of a single-layer graphene is low (2.3%)[24,81]. The integration of graphene with waveguide structures enhances its light absorption through evanescent field coupling. Following this approach, graphene-integrated waveguide photodetectors were first introduced in 2013[111-113]. Gan *et al.* demonstrated a graphene-integrated waveguide photodetector with the structure schematically shown in Fig. 5(a)[111]. Using a metal-doped graphene junction coupled evanescently to the waveguide [Fig. 5(b)], the detector was working under the PV mode and achieved a responsivity above 0.1 A W^{-1} across 1450 to 1590 nm spectra, as well as an over 20 GHz response rate and a 12 Gbit/s optical data link at zero bias. Simultaneously, Wang *et al.* reported an NIR to MIR responding photodiode with a similar graphene-integrated Si waveguide structure [Fig. 5(c)][112]. The evanescent light absorption in graphene, together with bias control in a graphene/silicon-heterostructure, contributed to a high responsivity of 0.13 A W^{-1} for 2750 nm light at room temperature. Obviously, the abundant electronic properties of graphene make it possible to be easily doped by the metal contacting and can form the heterostructures with waveguide semiconductors, which lay the structural foundations for PV devices. Since then, graphene-integrated PV photodetectors developed rapidly, and a 3 dB bandwidth exceeding 40 GHz and data rates up to 50 Gbit/s were achieved[78,114]. PC and PG photodetectors, with their characteristics of high photoconductive gains and high responsivity, are another important direction. In 2022, Jiang *et al.* proposed a graphene-integrated PG detector [Fig. 5(d)][115]. With the enhanced photogating effect established by potential fluctuation

engineering at the graphene/Si-waveguide interface [Fig. 5(e)], the device reached a responsivity of 240 A W^{-1} at 1550 nm wavelength. Constrained by inherent operating mechanisms of PC and PG, these devices exhibit inferior response speeds [Fig. 5(f)], which may not be suitable for high-speed PICs applications.

The strong electron–electron interactions facilitate the hot carriers' multiplication and result in a large Seebeck coefficient in the graphene[116]. In addition, the large optical phonon energy (~0.2 eV) and the low scattering rate via acoustic phonons give rise to an increased temperature of hot carriers within picoseconds[117-120], making the PTE effect an important role in graphene-integrated photodetectors with the potential for high responsivity and high-speed performance[119,120]. In 2016, Schuler *et al.* presented a PTE graphene photodetector integrated on a silicon slot waveguide, which acts as a dual gate to create a p−n junction in the optical absorption region of the device [Fig. 6(a)][121]. Extrinsic responsivities of 35 mA/W at zero bias and 76 mA/W at 300 mV bias voltage were achieved. The 3 dB bandwidth of the device is 65 GHz. Later, in 2021, Schuler *et al.* improved the PTE graphene photodetector by integrating graphene with Si microring resonators[122], as shown in Fig. 6(b), achieving > 90% light absorption [Fig. 6(c)] in ~6 µm SLG and a voltage responsivity of ~90 V/W. In addition to the PTE effect, graphene has a small electron heat capacity and weak electron-lattice coupling[123–125], leading to a large light-induced change in the electron temperature, and thus giving graphene the capacity to achieve the PBE effect[124,126–129]. In 2020, Gosciniak *et al.* proposed a graphene PBE detector based on a hybrid waveguide that allows for a high responsivity on the scale of hundreds of A/W and high-speed on the scale of hundreds of
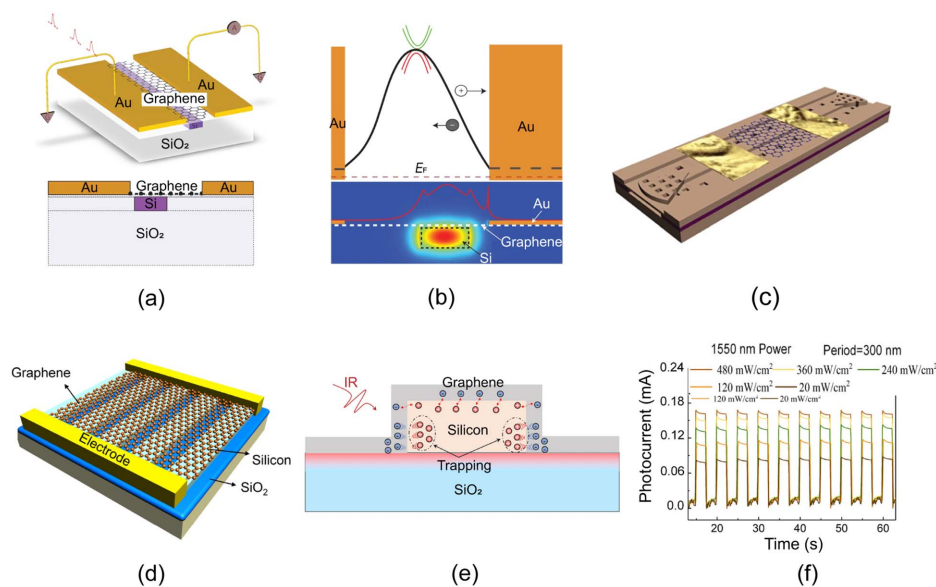
Fig. 5. (a) Schematic of the waveguide-integrated graphene photodetector. (b) Potential profile (black solid line) across the graphene channel. (a) and (b) Reproduced with permission[111]. (c) Schematic of graphene/silicon-heterostructure waveguide photodetector. Reproduced with permission[112]. (d) Schematic of the graphene-integrated PG detector. (e) Schematic diagram of the enhanced electric field on the separation of photogenerated carriers in the graphene. (f) Photoswitching characteristics of the device. (d)–(f) Reproduced with permission[115].

GHz[124]. The realization of high response speeds beyond hundreds of GHz can be attributed to the fast response time of the hot carriers in the graphene. It also needs to be emphasized that the response mechanisms may be complex in some situations. Guo et al.'s devices showed the PTE effect dominating the photoresponse under zero bias, while the PBE/PC effects become dominant when bias voltage is applied [Fig. 6(d)][88]. These works pave the way toward the wide use of PTE and PBE graphene-integrated photodetectors in PICs for high-speed applications by leveraging the hot carrier properties of graphene.

While there have been significant achievements in graphene-integrated photodetectors, there are still some shortcomings that need to be addressed and optimized before their broader adoption in PICs. First, the gapless band structure of graphene causes side effects of the relative larger dark current and the NEP. Some strategies have been put forward to suppress the dark current, such as tuning the E_f of graphene at the Dirac point for increasing the graphene series resistance, simultaneously boosting the interband optical absorption of the graphene to enhance the device responsivity[88]. Incorporating graphene with other semiconductors, such as BP and hBN in the heterojunctions, is also a good solution to reducing dark currents[130,131]. Second, the insufficient light absorption in graphene also impedes the promotion of responsivities in the PV/PTE photodetectors. Graphene plasmon effects have also been exploited[88,124,126,127,132,133,134]. For example, Vangelidis et al. raised the plasmonic-assisted light absorption in graphene based on the traditional asymmetrical metal contact graphene/Si-waveguide architecture [Fig. 6(f)][133]. Yan et al. demonstrated a novel graphene integrated double slot plasmonic

structure supporting a high-performance photodetection of 603.92 mA/W and a large bandwidth of 78 GHz [Fig. 6(e)][132].

Finally, we would like to emphasize the adaptability of graphene integration in Si_3N_4[135], thin-film lithium niobate (TFLN) platforms[136,137], as well as the scalability to large-area PICs[72,135,138]. In 2019, Giambra et al. demonstrated the first graphene-integrated Si-waveguide modulators with a 29 GHz EO bandwidth and a 50 Gbit/s modulation speed, relying on wafer-scale seeded array fabrication methods and CMOS compatible processes[72]. In 2021, they extended the scope of wafer-scale graphene integration on a 150 mm Si_3N_4 platform[135]. Updated in 2023, Wu et al. developed the wafer-scale integration process for realizing graphene-based photonic devices in a 300 nm CMOS pilot line[138]. By using Fab-level integration and process optimization, they achieved the modulation depth of 50 ± 4 dB mm⁻¹ and the EO bandwidth of 15.1 ± 1.8 GHz on 400 device measurements. The high reproducibility, high-volume, and low-cost manufacturing enabled by Fab technologies paved the way for graphene-integrated PICs mass production and practical applications to the market[138].

3. TMDC-Integrated PICs

3.1. Optoelectronic basics of TMDCs

TMDCs are an emerging class of 2D materials in a chemical formula of MX_2, where M represents the transition metal (Mo, W, etc.), and X is the chalcogen atom (S, Se, and Te). Four representative TMDCs have been sufficiently studied and implemented in PICs applications: molybdenum disulfide (MoS_2),
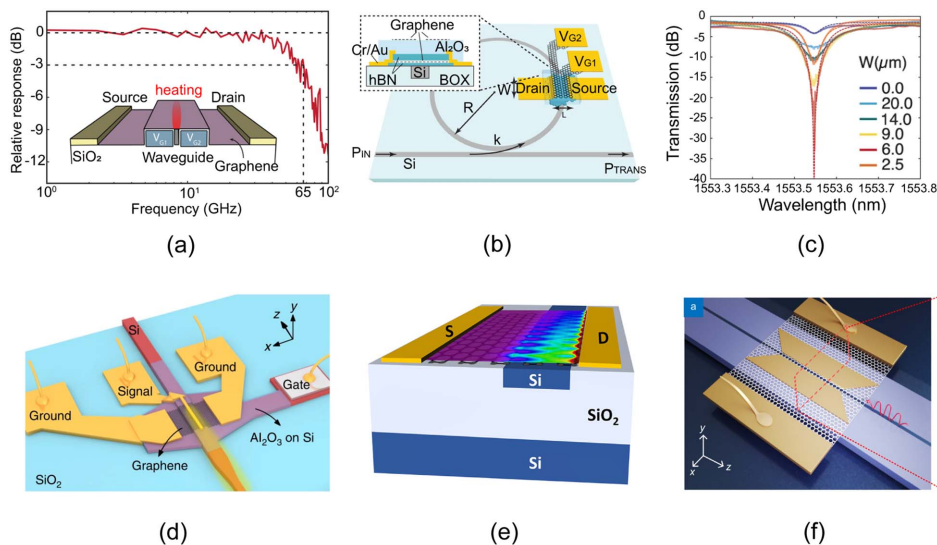
Fig. 6. (a) Measured frequency response of the graphene photodetector based on a slot waveguide plotted in the inset. Reproduced with permission[121]. (b) Sketch of the Si microring resonator integrated graphene photodetector and (c) its transmission spectra. (b) and (c) Reproduced with permission[122]. (d) Schematic of the Si-graphene hybrid plasmonic waveguide photodetector. Reproduced with permission[88]. (e) Schematic of the plasmonic device configuration with graphene and the Si waveguide. Reproduced with permission[132]. (f) Schematic of the plasmonic photodetector based on graphene and the double-slot structure. Reproduced with permission[133].

molybdenum diselenide (MoSe$_2$), tungsten disulfide (WS$_2$), and tungsten diselenide (WSe$_2$).

In 2017, Manzeli *et al.* reviewed the structures and electronic properties of TMDCs[26]. Generally, in terms of different stacking orders (chalcogen-metal-chalcogen), TMDCs have two structural phases: trigonal prismatic (2H) and octahedral (1T) [Fig. 7(a)]. The four common TMDCs are thermodynamically stable at the 2H phase. Take MoS$_2$ as an example; its calculated electronic band structure is given in Fig. 7(b). The indirect bandgap in the bulk material turns into a direct bandgap semiconductor monolayer. The bandgaps of these four monolayer TMDCs are in a range of 1.0 to 2.5 eV[139]. In addition to varying atomic layers, introducing element defects and constructing van der Waals connection with other 2D materials are other potential approaches to TMDCs bandgap engineering[26,139–141]. The electronic mobility in TMDCs is not as high as graphene, in the range of tens to hundreds of cm^2 V^{-1} s^{-1}, which might be owing to the remote optical phonons and Coulomb scattering from the interfacial charge traps in the TMDC atomical thin layers[26]. The direct bandgap transition gives the monolayer TMDCs greater optical absorption (> 10%) and emission in the spectrum region from the VIS to the NIR, as well as stronger light–matter interactions than Si and Ge[26,141]. Because monolayer TMDC absorption is stronger than graphene, it promises a higher responsivity in photodetectors [Fig. 7(c)][139,141]. Moreover, monolayer TMDCs exhibit large excitonic bonding energies[142,143], resulting in distinguished photoluminescence

(PL) properties [Fig. 7(d)][144]. The PL lifetime is ultrashort (ps), making TMDCs outstanding candidates in laser applications for optical communication. Lastly, the lack of inversion symmetry structures enables TMDCs potential in nonlinear optical applications[145–147].

3.2. TMDC-integrated lasers

Laser sources are essential components in PICs for providing light but generating on-chip lasers in Si is challenging due to the indirect bandgap, which hinders efficient light emission. Heterogeneous integration offers a solution. In particular, the recent emergence of 2D materials integration has tremendous potential for enabling efficient on-chip lasers at the nanoscale. TMDCs with excitonic characteristics and resultant remarkable light emission properties have been extensively explored as gain media for laser applications in PICs.

The conditions for realizing lasers are much stricter than other light sources, such as light-emitting diodes (LEDs). First, lasers typically operate based on stimulated emission rather than spontaneous emission, as seen in LEDs. Second, the population reversion in gain materials is the perquisition for producing lasers, i.e., the probability of stimulated transition should be higher than that of the spontaneous emission. Last but not the least, a resonant cavity is essential to consolidate the frequencies and phases of emitted light, ultimately amplifying it into coherent light. In this situation, the Q-factor of the
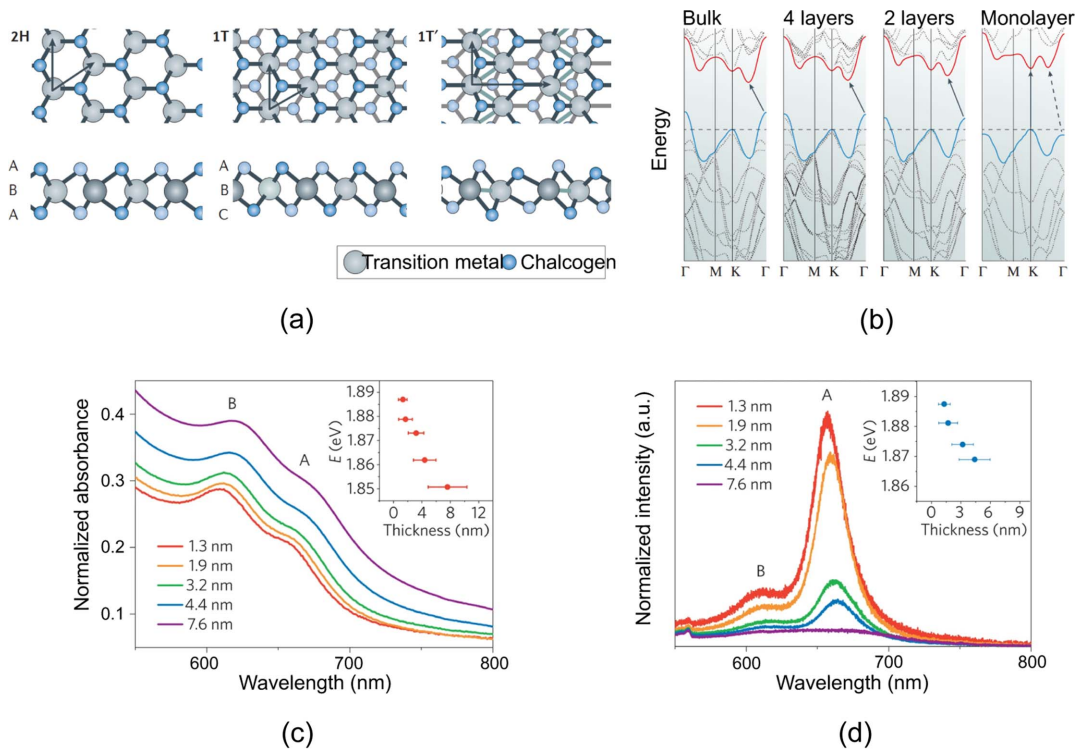

Fig. 7. (a) Atomic structure of the single layers of the TMDCs. (b) Evolution of the band structure of 2H-MoS$_2$ calculated for samples of decreasing thickness. (a) and (b) Reproduced with permission[26]. (c) Absorption and (d) photoluminescence spectra of the MoS$_2$ thin films with average thicknesses ranging from 1.3 to 7.6 nm. (c) and (d) Reproduced with permission[144].

resonant cavities is important for acquiring the gain for the lasers. The other specifications of a laser include the lasing threshold, the full-width at half-maximum (FWHM), and the beta factor (β).

In 2015, Wu *et al.* reported the first nanoscale laser system based on 2D monolayer WSe$_2$[148], whose structure is illuminated in Fig. 8(a). The monolayer is directly transferred and coupled to an L3 type PCC on a gallium phosphide (GaP) thin membrane. The holes in the L3 PCC is specially designed so that the highest Q-value mode is resonant with the monolayer PL peak at ~740 nm [Fig. 8(b)]. They recorded an optical pumping threshold of 27 nW at 130 K with a linewidth of 0.3 nm. Ge *et al.* proffered a room-temperature laterally confined photonic-crystal surface-emitting laser (PCSEL) incorporated with the

monolayer WS$_2$[149], but the emission wavelength is still in the VIS region. As an alternative to PCCs, the resonant microdisk that works in the whispering gallery mode with a high Q-value and strong optical confinement is appealing for use as light sources in PICs.

In 2015, Ye *et al.* reported a monolayer WS$_2$ excitonic laser in a microdisk resonator [Fig. 8(c)][150]. They embedded the monolayer between two dielectric microdisks [Si$_3$N$_4$/WS$_2$/hydrogen silsesquioxane (HSQ)], leading to a visible emission at 612.2 nm [Fig. 8(d)] with a Q-value of ~2604. This unique sandwich structure also produced a relatively low-lasing threshold of ~5–8 MW cm^{-2} pump intensity. Similarly, Salehzadeh *et al.* demonstrated SiO$_2$ sphere/multilayer MoS$_2$/SiO$_2$ disk-structured lasers[151], exhibiting multiple lasing peaks in the
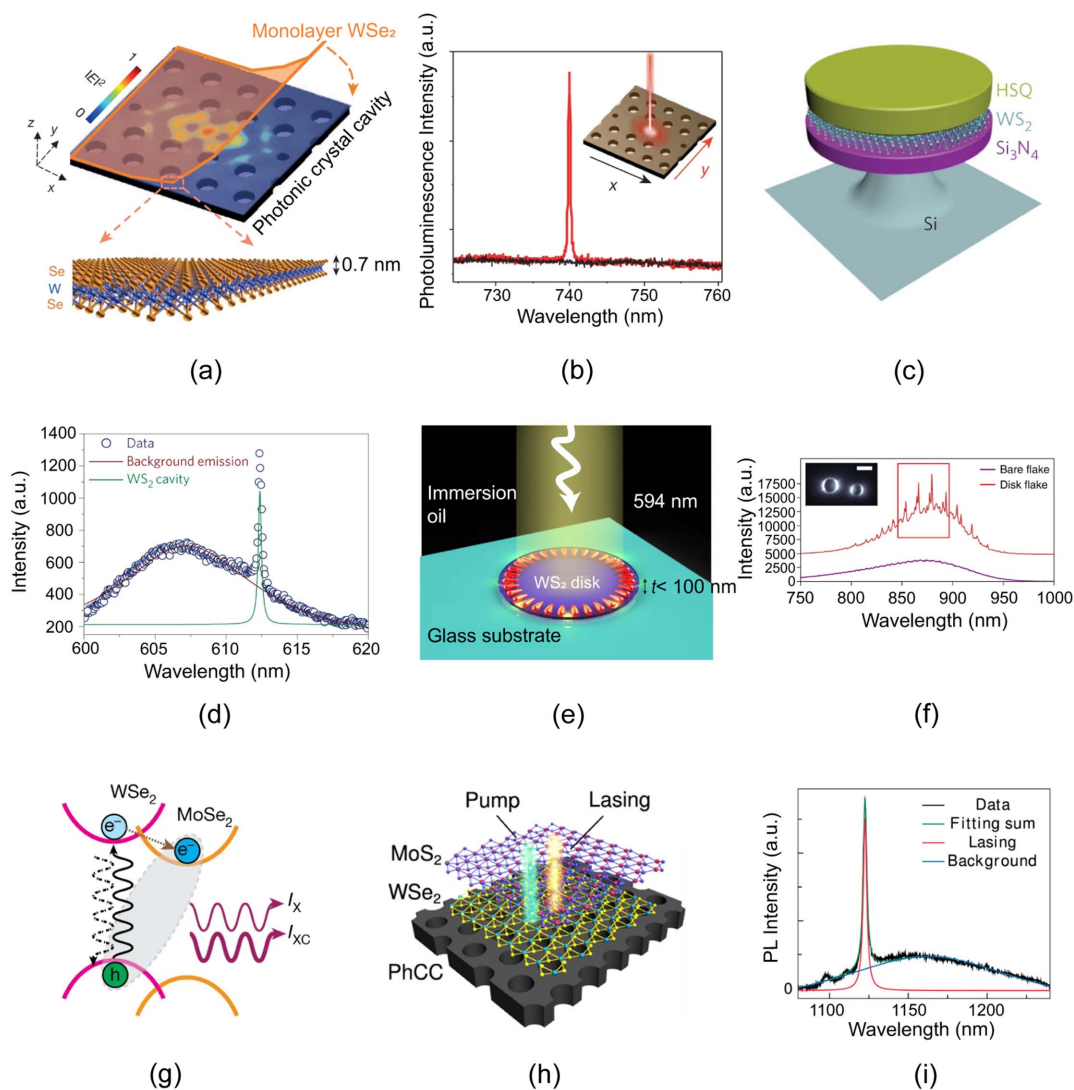
Fig. 8. (a) Schematic of the hybrid monolayer WSe$_2$-PCC nanolasers and (b) their PL spectrum. Reproduced with permission[148]. (c) Schematic image of a monolayer WS$_2$ microdisk laser and (d) its PL spectrum. (c) and (d) Reproduced with permission[150]. (e) 3D schematic image of an optically pumped WS$_2$ disk nanolaser and (f) its emission spectrum. Inset: emission image. Reproduced with permission[154]. (g) Type-II band alignment and carrier dynamics of the heterobilayer. Reproduced with permission[158]. (h) 3D schematic image of the heterobilayer-PhCC nanolaser. (i) Cavity lasing emission as compared to the heterobilayer PL background. (h) and (i) Reproduced with permission[159].

wavelength range of ~600 to 800 nm and line width of 0.36 and 0.26 nm. The threshold is measured to be ~5 μW. Reed *et al.* creatively designed a spatial notch on the SiO_2 microdisk covered by the bilayer MoS_2, which enables easy out-coupling of emission[152]. In 2018, Duong *et al.* transplanted the WSe_2 monolayers and integrated them on the Si_3N_4 circular Bragg grating structures[153], producing a record high contrast of the spin valley readout (> 40%). Recently, in 2022, Sung *et al.* published an interesting work about the observation of unexpected indirect-bandgap transition lasing in a 50-nm-thick WS_2 disk [Figs. 8(e) and 8(f)][154]. The whispering gallery modes in the WS_2 disk resonators offer sufficient optical gain for lasing action, breaking prerequisite limits of direct-bandgap transition semiconductors for lasers.

However, the abovementioned works have all resulted in lasers with wavelengths in the VIS region and are limited by the bandgap of the selected TMDCs. It is important to extend the wavelength of the TMDCs-integrated lasers into the NIR spectrum, which would be highly valuable for applications in PICs, especially optical communication. The first option is to exploit the $MoTe_2$ with a relatively smaller bandgap of ~1.1 eV for on-chip lasers[155–157]. Much research has been conducted to integrate the monolayer, the bilayer, and the multilayer $MoTe_2$ with the photonic PCC or nanobeam structures to achieve infrared lasers with wavelengths of up to 1305 nm. These lasers can be applied in the O-band datacom and offer room temperature operation, making them compatible with photonic integrated circuits (PICs) for practical applications[155–157]. Moreover, it has been demonstrated that the energies of the interlayer excitonic emissions in the TMDCs heterojunctions (Type-II band alignment) are lower than those of the intralayer excitonic emissions [Fig. 8(g)][158], providing opportunities to achieve a red shift in the emitted wavelength in the TMDCs heterojunctions. Liu *et al.* reported an interlayer exciton laser at 1122.5 nm with MoS_2/WSe_2 heterostructures [Figs. 8(h) and 8(i)][159]. Paik *et al.* demonstrated infrared lasing based on $WSe_2/MoSe_2$ heterostructures[158]. It is worth mentioning that the longer lifetime of the interlayer excitons also expedites a higher probability of population reversion in stimulated emission.

Although tremendous progress has been made in TMDCs and 2D material-integrated optical-pumped lasers, electrically pumped lasers based on 2D materials have not been achieved yet, which is more vital and urgent in PICs applications. Moreover, while TMDCs-integrated on-chip lasers have demonstrated prominence in the spectrum range from VIS to approximately 1.3 μm, extending the operating wavelength to cover other datacom and telecom regions remains a challenge. Nevertheless, we remain confident that with the advancement of nanotechnologies, such as bandgap engineering[160] and van der Waals heterojunctions of 2D materials[161], these gaps could be adequately addressed.
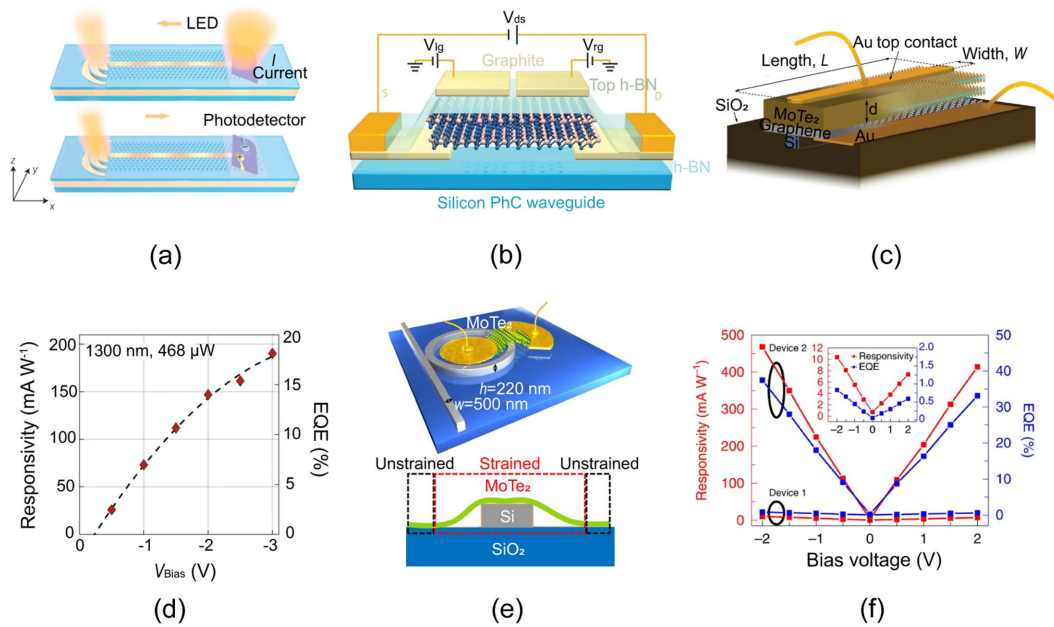
3.3. TMDC-integrated photodetectors

TMDC-integrated photodetectors that exhibit a high responsivity and a low dark current can be considered important branches

that compliment graphene-integrated photodetectors ascribed to the strong light absorption (> 10%), the intensive light–matter interactions, and the reasonable bandgaps of TMDCs. TMDCs were first carried out on space light phototransistors[162–164]. Then, they were eagerly incorporated with waveguide-integrated photodetectors for the use in PICs. In 2017, Bie *et al.* fabricated a versatile $MoTe_2$-integrated Si PhCW-based device[155], which allows for both functionalities of LEDs and PV photodetectors. This ingenious device structure is illustrated in Figs. 9(a) and 9(b). The p–n junction in the bilayer $MoTe_2$ is electrostatically induced by the split graphite gates at the top, then is encapsulated by the hBN, and evanescently coupled to the modes of the PhCW at the bottom. This prototype exhibited a responsivity of 4.8 mA W^{-1} and an external quantum efficiency (EQE) of 0.5% at a wavelength of 1160 nm in the photodetection mode. In 2018, Ma *et al.* presented a graphene/$MoTe_2$/hBN waveguide-integrated photodetector for a more particular use[165]. The device was operable across the entire optical telecommunication O-band, with a responsivity of 23 mA W^{-1} and a bandwidth approaching 1 GHz. In 2020, Flöry *et al.* demonstrated a vertical $MoTe_2$/graphene heterostructure photodetector integrated with planar Si-waveguides[166] [Fig. 9(c)]. The use of a vertical heterostructure and an electrical field remedies the long transit times of carriers in the TMDCs, leading to a high speed (extrapolated 3 dB roll-off frequency ~50 GHz) and a high responsivity [200 mA W^{-1} at 1300 nm, Fig. 9(d)].

TMDCs and their heterojunctions can also be compatible for other PIC platforms[167–169]. For example, the monolayer MoS_2 and graphene/hBN/graphene/MoS_2 heterojunctions[167] have been integrated on Si_3N_4 photonic platforms with high on/off current ratios larger than 10^4, a responsivity of ~0.24 A W^{-1}, and a bandwidth of 28 GHz. In 2020, Maiti *et al.* reported an intriguing strain-engineered photodetector that heterogeneously integrated a multilayer 2H-$MoTe_2$ crystal flake atop a Si microring resonator (MRR) [Fig. 9(e)][160]. The strong localized strain introduced by the waveguide step resulted in a graded bandgap of $MoTe_2$ to below 1 eV, making TMDC-integrated photodetectors workable in the telecom C-band for the first time. Additionally, this device is outstanding, as it has features such as a strong responsivity of 0.5 A W^{-1} [Fig. 9(f)] and a hundred-fold reduction in dark current compared with graphene-integrated photodetectors and results in a low NEP of 90 pW $Hz^{-0.5}$.

Even great progress has been made in TMDC-integrated photodetectors. They are far from being perfect enough to boast about their use in PICs. First, the light absorption of TMDCs drops dramatically with the red shift of the wavelength [Fig. 7(c)], leading to a relatively low infrared responsivity compared with their performance in the VIS. Forming TMDC heterostructures with other low bandgap 2D materials such as BP might be a good solution. Second, the mobility of the monolayer TMDCs is highly sensitive to environmental factors and degrades significantly without protections[26]. 2D insulators, such as hBN and hafnium oxide (HfO_2), can be excellent options

Fig. 9. (a) Design of the waveguide-integrated LED and photodetector. (b) Cross-sectional schematic of the encapsulated bilayer MoTe$_2$ p–n junction on top of a Si-PhCW. (a) and (b) Reproduced with permission[155]. (c) Schematic illustration of a vertical MoTe$_2$-graphene heterostructure detector coupled to a silicon waveguide buried in SiO$_2$ claddings. (d) Simultaneously measured responsivity and the corresponding EQE as a function of the applied bias voltage. (c) and (d) Reproduced with permission[166]. (e) Schematic and cross-sectional view of an MRR-integrated MoTe$_2$ photodetector. (f) Responsivity and EQE as a function of the bias voltage of the device. (e) and (f) Reproduced with permission[160].

to encapsulate TMDCs for propelling TMDC-integrated devices into a real use.

## 4. Black Phosphorous-Integrated PICs

4.1. Optoelectronic basics of BPs

Black phosphorus (BP), an emerging 2D material with a small bandgap and the VIS to MIR operation, is considered to bridge the wavelength gap between graphene and TMDCs[170]. BP has an orthorhombic crystalline structure similar to graphene, where phosphorus atoms are arranged in a honeycomb lattice [Fig. 10(a)]. Different from graphene and other 2D nanomaterials with flat atomic planes, BP is formed by buckled double layers, which determine a series of anisotropic physical properties of BP[171]. Electrically, BP has a varied direct bandgap of ~0.3 eV in bulk and ~2 eV for the monolayer[170,172]. The preserved direct bandgap, regardless of layer numbers, is distinct from indirect-direct transitions of TMDCs [Fig. 10(b)], facilitating light–matter interactions of BP. In addition to changing layer thickness[173], electrical control[174], chemical tailoring/doping[175,176], and strain engineering[177,178] are also effective ways to tune the bandgap of BP. Moreover, BP presents a high carrier mobility of over 1000 cm^2 V^{-1} s^{-1} [171,179]. BP is not comparable to graphene, but it outperforms TMDCs in PICs applications with larger current on/off ratios. BP displays strong doping and thickness-dependent optical properties [Fig. 10(c)]. The absorption edge of BP is layer thickness dependent, ranging

between 0.3 and 0.6 eV with decreasing thickness attributed to the quantum confinement enlarged energy gap[171]. The PL spectra follow the same phenomenon [Fig. 10(d)]. The PL peak red shifts as the BP layer thickness is reduced[180,181]. In summary, the tunable electronics and ultrabroad (VIS-MIR) optics of BP make them excellent choices for potential use in photonic applications[182–184].

4.2. BP-integrated photodetectors

In 2015, Youngblood *et al.* exfoliated multilayer black phosphorus from bulk crystal and transferred it onto one of the optical arms of the MZI to fabricate photodetectors [Fig. 11(a)][130], which can be operating in the NIR telecom band. Graphene, on top of BP with an Al$_2$O$_3$ dielectric interlayer, serves as a gate to control the conductance of the BP and forms a PV-type phototransistor evanescently coupled with the underearth Si-waveguide. Unlike graphene-integrated photodetectors, which suffer from high dark current, BP devices presented very low dark current under bias while attaining an intrinsic responsivity of up to 657 mA W^{-1} (100-nm-thick device) and a bandwidth exceeding 3 GHz [Fig. 11(b)]. Subsequently, their group proposed a PC effect-dominated BP photodetector integrated on the Si photonic platform[185], showing a responsivity 10 A W^{-1} afforded by internal gain mechanisms, and a 3 dB roll-off frequency of 150 MHz. Similar to TMDCs, 2D BP is susceptible to the atmosphere and should be carefully encapsulated for the practical use. Oxide dielectric layers[130], polymer cladding[186], and 2D
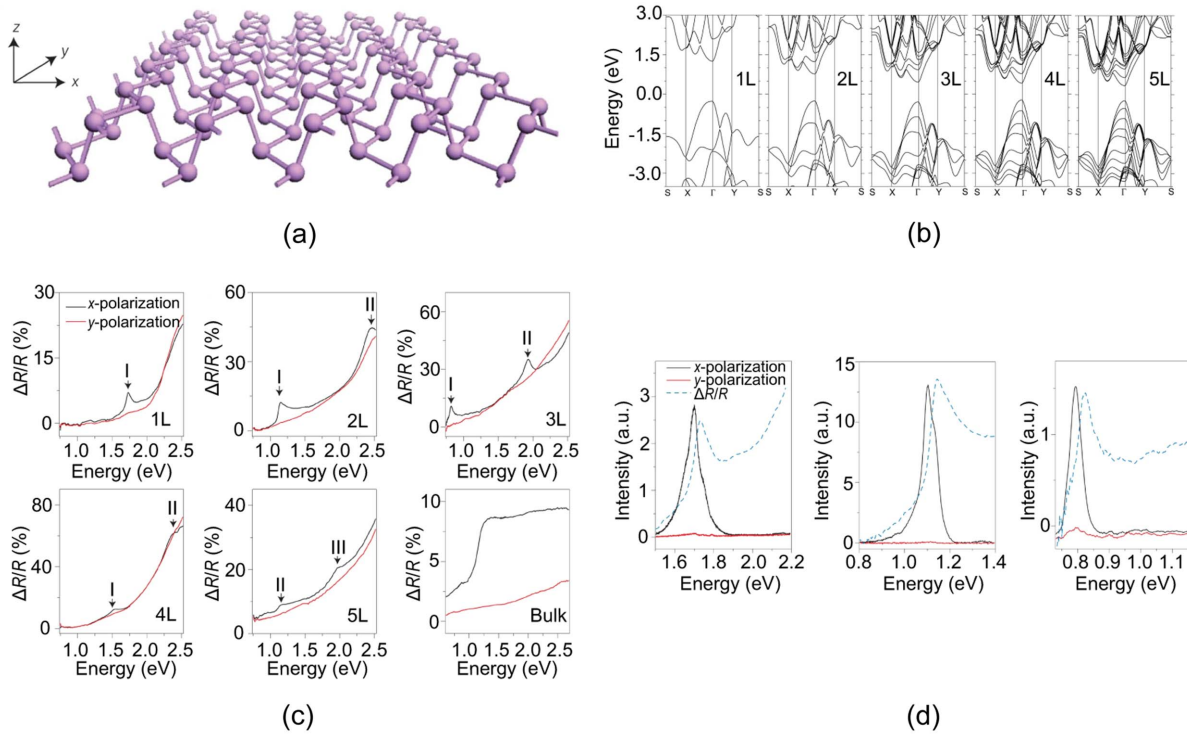
Fig. 10. (a) Puckered honeycomb lattice of the monolayer phosphorene. *x* and *y* denote the armchair and zigzag crystal orientations, respectively. (b) Band structures for different few-layer phosphorene systems obtained from HSE06 hybrid functional calculations. Reproduced with permission[172]. (c) Reflection spectra of the monolayer, bilayer, trilayer, tetralayer, and pentalayer phosphorene. (d) PL spectra of the monolayer, bilayer, and trilayer phosphorene. (a), (c), and (d) Reproduced with permission[181].

insulators hBN and HfO_2[187] are common media used in device structures to protect BP from moisture.

Although the small bandgap of BP enables the operation of photodetectors in a broadband from VIS to MIR, the intrinsic weakened light absorption of BP in the infrared region [Fig. 10(c)] diminishes the device's responsivity. Diverse photonic structures, benefiting from the flexibility of optical designs in PICs, have been explored for integration with BP for device performance breakthrough[188,189]. For instance, Ma *et al.* proposed a PC-dominated BP photodetector on a 10 μm-long PhCW by using slow-light effects [Fig. 11(c)], achieving a 11.31 A W^{-1} responsivity and a 0.012 nW Hz$^{-1/2}$ NEP[188]. Tian *et al.* reported the integration of a BP photodetector with the planar PCC to strengthen the BP light–matter interaction lengths [Fig. 11(d)][189]. Recently, metasurfaces that boost light absorption through resonant or plasmonic effects, have become attractive for use in infrared photodetection. In 2022, Lien *et al.* used resonant metal-insulator-metal (MIM) metasurface gratings to increase MIR absorption and responsivity when integrating them with a thin-film BP photodetector[190]. Yadav *et al.* designed an Au disk-based plasmonic metasurface integrated into BP photodetectors [Fig. 11(e)][191] to achieve a peak responsivity of 495.85 mA W^{-1} and an ultrahigh operation speed (> 10 MHz) at the power of 8.55 μW under a 3.7 μm incident wavelength. Improving the MIR responsivity is challenging due to the intrinsic material optical properties constrain in the

infrared. It is believed that new resonant structures and metasurface designs in PICs offer new path toward high-responsivity BP MIR photodetecting.

Lastly, we want to emphasize the compatibility of BP integration to diverse PIC platforms by an example[190,192]. BP photodetectors based on TFLN have been reported with a high extrinsic responsivity of 148 mA W^{-1} measured at 1550 nm wavelength under a low bias of 0.3 V [Fig. 11(f)][192].

5. hBN-Integrated PICs

5.1. Optoelectronic basics of hBN

hBN plays a crucial role in the 2D materials family due to its exceptional optoelectronic, mechanical, and thermal properties. It serves various functions in 2D material-based devices, such as insulators, dielectric interlayers, and encapsulations[31,193,194]. The atomic structure of hBN is quite similar to graphene [Fig. 12(a)], in which boron and nitrogen atoms are alternately arranged, leading to some resemblances to the properties of graphene, such as the moiré superlattice in the twisted bilayer hBN[195–198]. Noticeably, hBN has an atomically smooth surface, is relatively free of dangling bonds, and also has chemical and thermal stability. It is well suited for 2D material heterogeneous substrates[36,196,199,200]. There is also solid evidence that hBN is a better dielectric choice than traditional SiO_2. Compared to
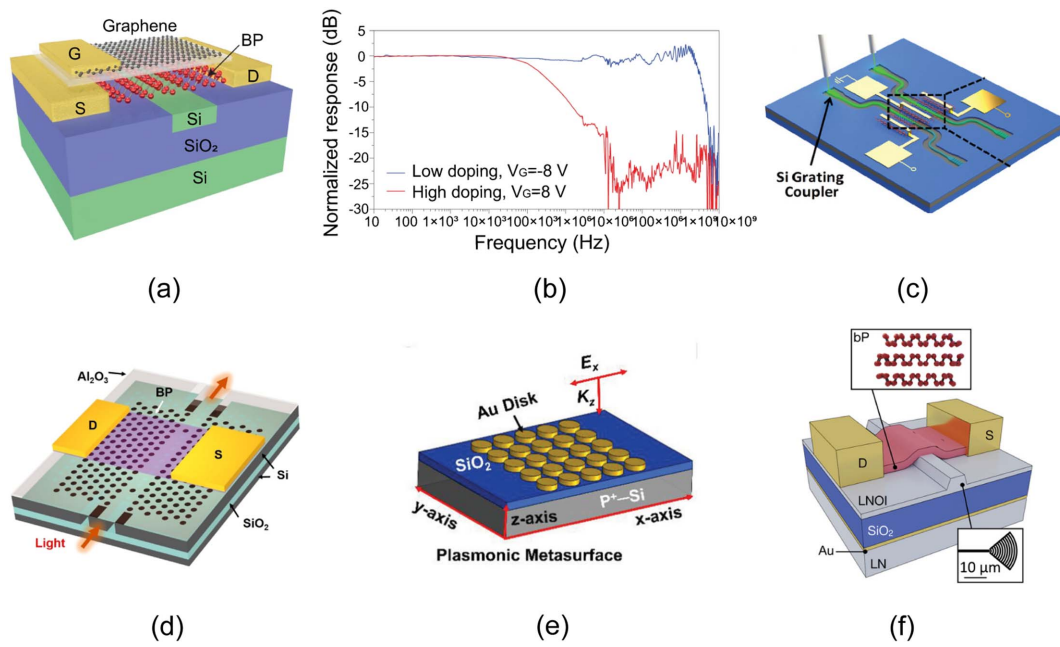
Fig. 11. (a) Schematic and (b) frequency response of the BP photodetector integrated in a Si PIC. Reproduced with permission[130]. (c) Schematic of the BP photodetector integrated in Si PhCWs. Reproduced with permission[188]. (d) Schematic of the BP photodetector integrated on a PPC cavity. Reproduced with permission[189]. (e) Schematic of Au disk-based plasmonic metasurface. Reproduced with permission[191]. (f) Schematic of the BP photodetector integrated in a ridge LN waveguide. Reproduced with permission[192].

devices fabricated directly onto SiO_2/Si, hBN provides graphene devices with almost one order of magnitude higher carrier mobilities because it reduces Coulomb scattering[36,201]. hBN has a relatively wide bandgap of ~6 eV to ensure its insulativity [Fig. 12(b)]. Corresponding to its large bandgap, the optical window of hBN is located at the ultraviolet (UV) region [Fig. 12(c)], with a PL emission at ~230 nm and a bandwidth around 300–400 meV [Fig. 12(d)][202], making hBN a promising material for applications in UV optoelectronics[198,203,204].

5.2. hBN-integrated heterostructure devices

hBN is typically used in the form of heterostructures with other 2D materials when it is integrated into PICs. The discussions above highlight that a single 2D material and its properties can hardly satisfy all the functionalities required from PICs. For example, TMDCs excel at VIS to NIR photodetection, and we may expect that BP can be integrated with TMDCs for a broadband from VIS to MIR photodetection. 2D material heterostructures, which combine different 2D materials via van der Waals connections, open a new avenue for heterogeneous integration in PICs and performance breakthrough[196,198,199,205–207]. First, 2D materials with their special layered atomic structures and absence of dangling bonds, can be vertically stacked and bonded using the van der Waals force, avoiding the influence of lattice mismatch that is troubling in conventional epitaxial heterogeneous integration. Second, the vertical heterostructures provide shorter carrier transport channels than lateral structures, from which carriers can be quickly

separated and collected. Lastly, in contrast to bulk junctions, 2D material heterostructures are constructed in the atomic thickness level, and carrier confinement makes a sharp built-in filed distribution, which is beneficial for the realization of a high-speed operation. From Sections 3.2, 3.3, and 4.2, we have seen the characteristics of hBN in heterostructures with other 2D materials. Here, we just review several typical works based on PICs and emphasize the roles hBN heterostructures play in these structures.

In 2015, Shiue et al. exhibited an hBN/graphene/hBN sandwiched PTE-type photodetector based on Si PICs using van der Waals assembly[131]. The device architecture is depicted in Fig. 13(a). Graphene is encapsulated by the hBN while coupling to the optical mode of a Si-waveguide. The mobility of hBN-encapsulated graphene can be reserved to 80,000 cm^2 V^{-1} s^{-1} by reducing scattering rates, which exceeds that of traditional semiconductors, such as Ge, by 1–3 orders of magnitude. Additionally, the one-dimensional contacts to the hBN/SLG/hBN stack combined with a wide channel design reduced the device resistance to as low as ~77 Ω. Both the reserved high mobility of the graphene and the lower device resistance benefited from the hBN/graphene heterostructures, which yielded a photodetector with the maximum responsivity of 0.36 A/W and a high-speed operation of 3 dB cutoff at 42 GHz [Fig. 13(b)][131]. In particular, capacitor structures are basic units in PICs for tuning the E_f of the graphene and other 2D materials. An hBN insulator can be an excellent partner for replacing SiO_2 in such structures. In this regard, the hBN/graphene heterostructures have been implemented in modulating
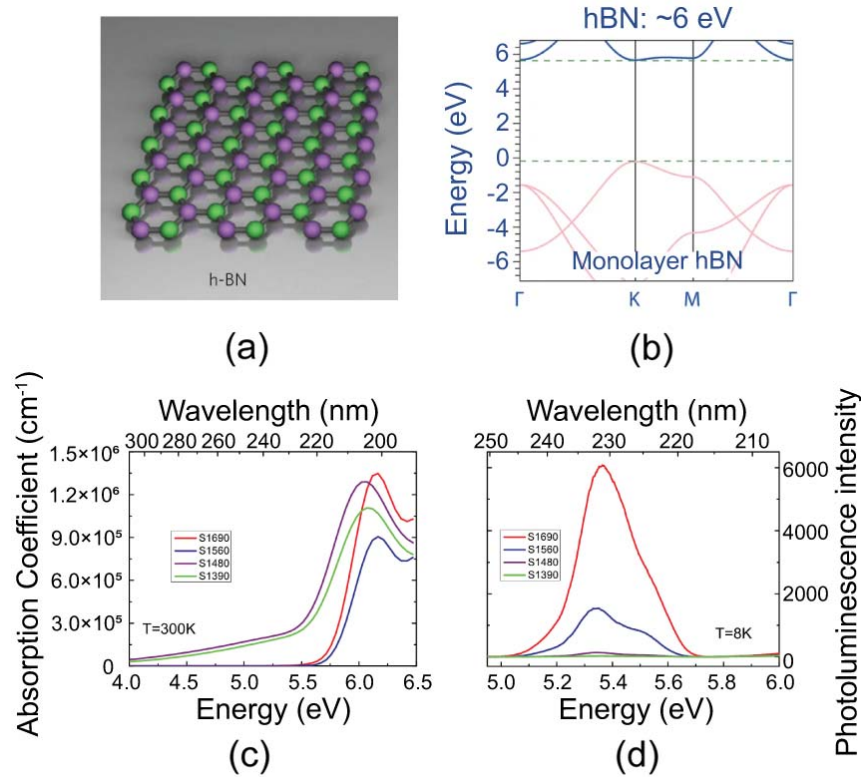
Fig. 12. (a) Schematic of the structure of the hBN. Reproduced with permission[197]. (b) Band structures of the monolayer hBN. Reproduced with permission[31]. (c) Absorption and (d) PL spectra in the hBN grown on sapphire. Reproduced with permission[202].

directions [Figs. 13(c) and 13(d)][208,209]. Fascinatingly, the magic twist angle and moiré superlattice reappear in hBN/graphene heterostructures, which creates new, finite-energy Dirac points in the graphene band structure and leads to the novel Hofstadter butterfly spectrum[196]. In 2021, Kuzmina *et al.* demonstrated twist-controlled resonant light emission from graphene/hBN/graphene tunnel junctions [Fig. 13(e)][210]. The emission peak lies in the NIR spectral region and can be tuned to over 0.2 eV [Fig. 13(f)], providing the zero-bandgap graphene with the capacity to act as a potential candidate for on-chip optoelectronics light sources. hBN is also used in other 2D material heterostructures, such as TMDCs and BP applied in PICs, as shown in examples in Sections 3.3 and 4.2, respectively. It should be noted that the van der Waals heterostructure is a broad concept and has a variety of choice materials, not limited to hBN, other 2D materials, 0D and 1D materials, and bulk substrates, which could be mixed for interacting and shaping into heterostructures[205–207,211].

6. Other 2D Material-Integrated PICs

Benefiting from rapid advances in nanotechnologies, a number of novel 2D materials have been discovered to address the increasingly diverse demands for enhanced hardware performance in fields, such as computing, sensing, and communication. In this section, we introduce some impressive 2D materials,

such as few-layered indium selenide (In_2Se_3), perovskite 2D structures, 2D metal carbides and nitrides (MXene), and graphdiyne. These materials exhibit fascinating optoelectronic properties and hold immense potential for applications in PICs.

Few-layered In_2Se_3 has emerged as an unconventional phase-change material (PCM) to be studied in electronic memory devices[212]. Compared to conventional antimony (Sb)-based chalcogenides and chalcogenide alloys and PCMs, few-layered In_2Se_3 exhibits ultrafast and energy-efficient phase-change characteristics[213]. Li *et al.* systemically analyzed the structure of two-layered In_2Se_3 [Fig. 14(a)] and their underlying atomistic transition pathways[213]. They found that the interlayer "shear glide" and isosymmetric phase transition between the α- and β-structural states contain low reconfigurational entropy [Fig. 14(b)], which can account for the reversible switching between the layered structures in a timescale of ns and a relatively lower phase transition temperature of 220°C (that of Sb-based PCMs is beyond 600°C). Finally, reversible all-optical switching was demonstrated in a In_2Se_3-integrated Si-MRR [Fig. 14(c)]. These results provided few-layered In_2Se_3 with larger potential use in large-scale memory devices and energy-efficient all-optical neurocomputing applications. Perovskites belong to a class of ionic semiconductors with remarkable optoelectronic properties, such as appropriate bandgaps, strong light absorptions, long photocarrier lifetimes, and high fluorescence yields, and have been intensively studied for applications in solar
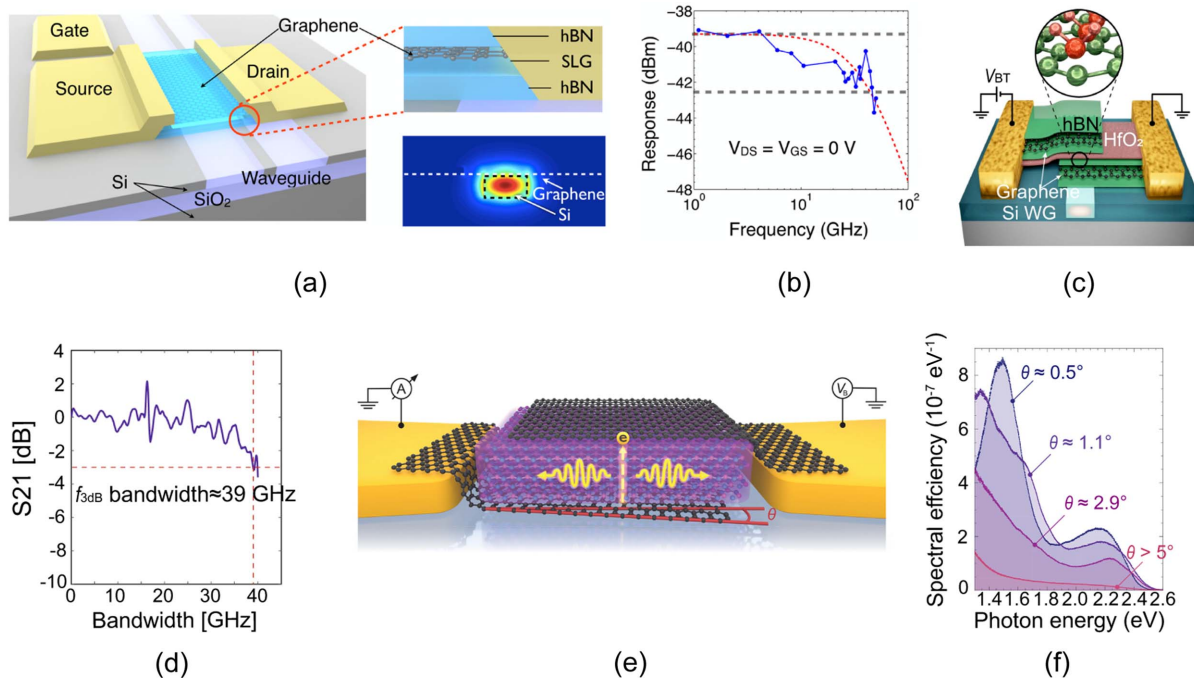
Fig. 13. (a) Schematic and (b) high-speed response of the hBN/SLG/hBN photodetector on a buried silicon waveguide. Reproduced with permission[131]. (c) Schematic cross-section and (d) electro-optical S21 frequency response of an EA modulator with an hBN/HfO₂/hBN dielectric. Reproduced with permission[209]. (e) Schematic of a twist-controlled Gr/hBN/Gr light-emitting tunnel junction. (f) Evolution of the spectral response for different twist angles θ. (e) and (f) Reproduced with permission[210].

cells, photodetectors, and LEDs[214,215]. The ease of chemical processing of perovskites enables the creation of various 2D forms, making them suitable for different application scenarios in PICs. For example, perovskite nanosheets revealing intrinsic nonlinear optical properties, can be used as an effective saturable absorber for the stable mode-locked pulse generation[214]. Perovskite microdisks integrated with Si₃N₄ PICs were fabricated into an on-chip laser [Fig. 14(d)][216]. It is interesting to investigate the combination of outstanding perovskite 2D materials with mature PIC platforms[217]. In addition, MXene and graphdiyne with their distinguished nonlinear saturable absorption effects[218,219] have also been implemented in versatile PICs applications, such as saturable absorbers[220], AO modulators[221], and on-chip photonic deep neural networks[222].

7. Integration Methods of 2D Materials with PICs

Despite the fact that 2D materials with their remarkable optoelectronic properties have made striking progress in PIC applications, their inherent mechanical fragility determines that caution should be used in the manipulation of 2D materials integrated with PICs and they may be difficult to mass production. The preparation methods of 2D materials have continued to evolve since their discovery, with mechanical exfoliation, liquid exfoliation, and chemical vapor deposition (CVD) growth being the most extensively investigated and matured techniques. Here, we provide an overview of these three major 2D materials, their

preparation approaches, and their subsequent integration methods in PICs.

It is well known that the initial discovery of graphene originated from tape mechanical exfoliation[25]. Subsequently, mechanical exfoliation has been established as a straightforward and versatile method for isolating 2D materials from their bulk crystals[223,224]. 2D materials are held together with neighboring atomic layers using weak van der Waals interactions, making them amenable to detachment from bulk crystals. Metal-assisted mechanical exfoliation is progressively supplanting tape-based methods, as it allows for higher throughput and can be adapted for wafer-scale production by harnessing the tensile stress-induced spalling between metal films and 2D materials[225,226]. Taking advantage of the different interfacial binding energy of the metals, graphene, TMDCs, BP, and hBN can be isolated by using selective metals[226,227]. Huang *et al.* developed a universal Au-assisted mechanical exfoliation method that can be applicable in 40 types of single-crystalline monolayers[223]. The mechanically exfoliated 2D materials with metal contacts can be directly transferred to wafers or other PIC substrates [take graphene as an example in Fig. 15(a)] to complete the target device fabrication[225]. While mechanically exfoliated 2D materials exhibit high quality, the precise control of their uniformity and shape on a large scale remains a challenge. This issue can significantly affect the subsequent integration process with PICs, especially when aiming at a standardized industrial process flow.
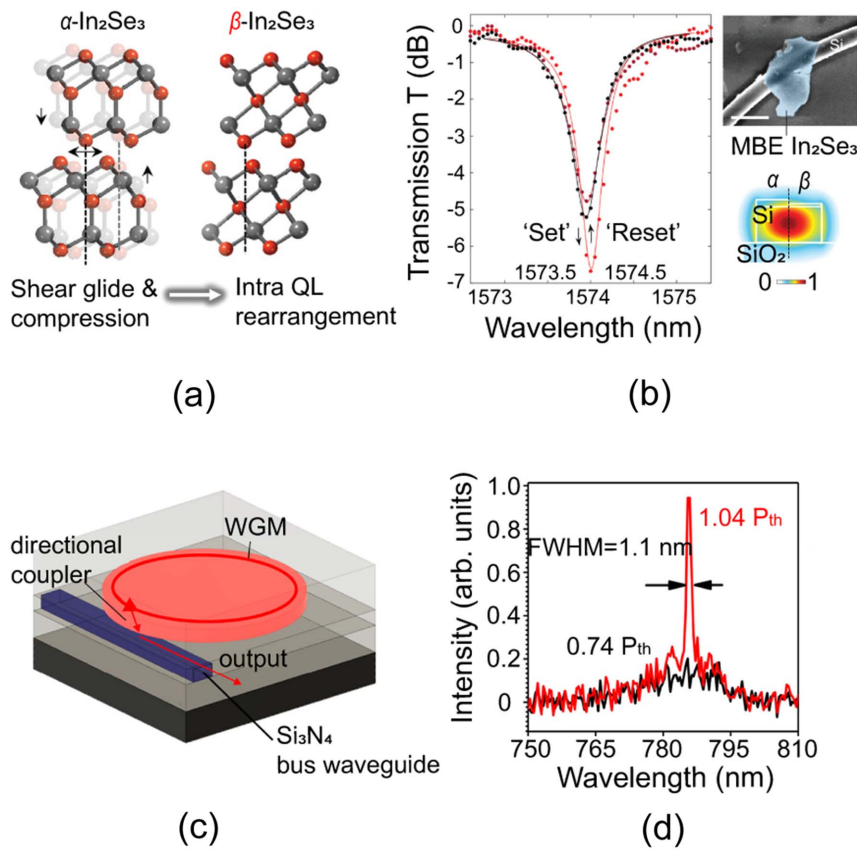
Fig. 14. (a) Atomic structure of α-/β-In$_2$Se$_3$ and (b) their transition process at room temperature. Left: normalized transmission spectra for the hybrid resonator with the $\alpha$-In$_2Se_3$ (black), β-In$_2$Se$_3$ (red), and retrieved α-state (dark red) In$_2$Se$_3$. Right: image and mode profile for the In$_2$Se$_3$ on the Si waveguide. (a) and (b) Reproduced with permission[213]. (c) Sketch and (d) Emission spectra of an MAPbI$_3$ disc laser integrated on a Si-nitride photonic chip. Reproduced with permission[216].

The next method for preparing 2D materials involves liquid exfoliation of bulk crystals. In addition to the mechanical shear forces, liquid exfoliation introduces a chemical fact that ions in liquids can be absorbed or exchanged into layer spacing for facilitating the isolation [Fig. 15(b)][228]. Assisted by sonication, a solvent containing 2D nanosheets is produced [Fig. 15(c)][229]. Meanwhile, graphene, TMDCs, BP, and hBN dispersed nanosheet solvents have been successfully realized by liquid exfoliation from their layered crystals[230]. Liquid exfoliation has some obvious advantages, including the ease of synthesizing a large quantity of nanosheets and straightforward size sorting through centrifugation, and most importantly, it facilitates the integration of 2D materials into PICs using well-established solution-based techniques, such as inkjet printing and roll-to-roll coating[229]. Inkjet printing is a promising process toward large-area integration with superiorities in material conservation, good controllability, and scalability. Noticeably, various 2D material heterostructures can be obtained using this technique[231–233]. It is also worth mentioning that inkjet printing is free of post patterning processes, which are essential in conventional 2D materials transfer methods. The nanosheets ink can be accurately printed on PIC chips without further mask preparations [Fig. 15(d)][233]. Pioneering work has been carried out in the inkjet printing of graphene and MoS$_2$ nanosheets onto an SOI substrate with a resolution of $\sim$80 µm[234]. However, several challenges must be addressed through further efforts to transition 2D materials inkjet printing into mass production, including solution concentration, patterning dimensions, jetting accuracy, and reliability in PIC applications.

In contrast to the exfoliation methods mentioned earlier, CVD growth is a bottom-up approach to preparing 2D materials. The process of CVD growth is not complex. Taking graphene as an example, a mixture of methane and hydrogen goes through Cu or Ni substrates at a temperature up to 1000°C in the furnace. Carbon atoms begin to seed on the substrates and then assemble into graphene readily. By adjusting gas species and reaction conditions, TMDCs and hBN are synthesized in the same manner[235–238]. It should be noted that the CVD method provides an approach to directly growing 2D materials on desired PICs structures[239], as well as *in situ* deposition of 2D material heterojunctions[240]. This holds significant value in simplifying the process of heterogeneous integration of 2D materials with PICs. While the CVD method may not yield 2D materials with the same surface area and mobility as those produced through mechanical exfoliation, it still excels in terms of layer and morphology control, which are critical factors
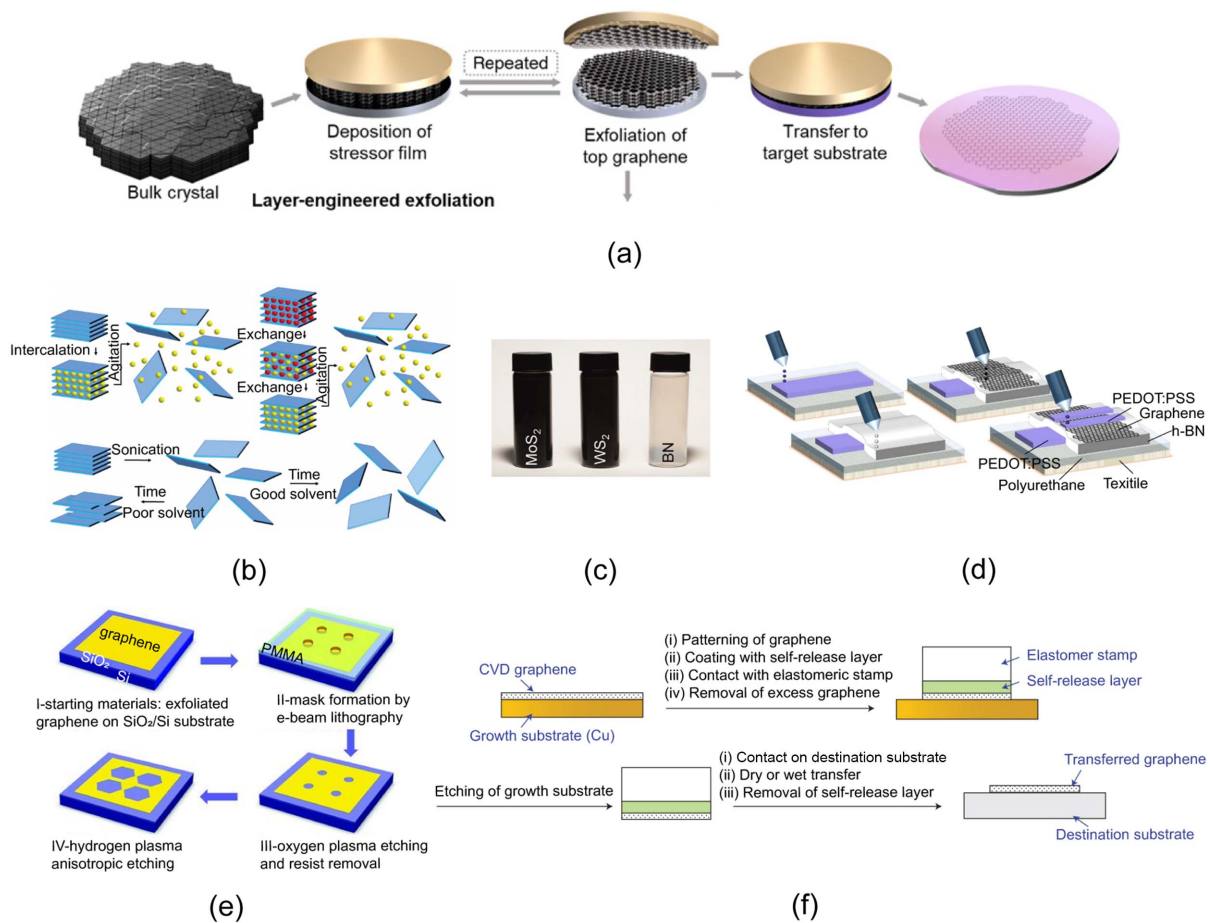
Fig. 15. (a) Schematic illustration of the graphene exfoliation technique. Reproduced with permission[225]. (b) Schematic description of the main liquid exfoliation mechanisms. Reproduced with permission[228]. (c) Photograph of the dispersion nanosheet solvent. Reproduced with permission[229]. (d) Schematic of inkjet-printing on a chip. Reproduced with permission[233]. (e) Schematic of the graphene patterning. Reproduced with permission[241]. (f) Schematic of the self-release layer (SRL) methodology in combination with a pick-and-place elastomer stamp. Reproduced with permission[242].

that influence device performance in PICs. It is important to note that CVD-grown 2D materials require metal substrates, necessitating a wet-chemical etching step to remove the metal.

Meanwhile, a polymer medium, such as poly(methyl methacrylate) (PMMA), is commonly employed to facilitate the transfer of 2D materials from a solvent onto the desired target substrates. The final but crucial step involves patterning the transferred 2D materials with the aid of lithography and dry etching. This process is essential for preserving the core area covered by 2D materials and removing excess portions to prevent optical losses [as illustrated with graphene in Fig. 15(e)]. An alternative transfer approach is using the polydimethylsiloxane (PDMS) stamp [Fig. 15(f)][242]. It allows patterning 2D materials before they are transferred to substrates. Additionally, some new techniques such as singular sheet etching[243], thermal annealing[244], EBL-direct-etching[245], and laser deposition[246] have been proposed for handling the integration of 2D materials into PICs more flexibly and carefully. Currently, enhanced by the innovation of synthetic methodologies and the optimization of integration processes, wafer-scale graphene[247], TMDCs[248], hBN[249],

and centimeter-scale BP[246] with high quality have been acquired, accelerating their applications in PICs.

8. Future Perspectives and Challenges

In the past two decades we have witnessed the emergence of 2D materials and their successful role in diversifying and boosting the performance of PICs. The integration of 2D materials with PICs has enticing and bright perspectives for embracing the era of "More than Moore's Law." First, it is foreseeable that the abundant physical, mechanical, and thermal properties of 2D materials would bring more sophisticated and "beyond traditional" functionalities into PICs to meet future application challenges, especially in the fields of next-generation computing and high-speed optical interconnection. Some frontier works have been reported. Graphene nanoheaters with highly efficient thermal conductive paths have shown great potential in ultralow energy consumption non-volatile devices[64]. MXene exhibiting nonlinear saturable absorption effects promises the realization

of on-chip photonic deep neural networks[222]. These works pave the way toward photonic and all-optical neuromorphic computing, which is widely regarded as the alternative approach to circumvent the von Neumann bottleneck[250]. Obviously, the potential of 2D materials has not been fully dug out. For example, from the above review, one can perceive that most of the 2D materials integrated into PICs handle light in the form of intensities and phases. There is plenty of room for introducing spin and linear light polarization manipulation into PICs to add their working capacities and degrees of freedom. Although some interesting works have shown polarization-sensitive photoresponse by integrating TMDCs with LiNbO$_3$[168,251], this functional novelty mainly comes from the spontaneous polarization structure of LiNbO$_3$ itself. In fact, 2D materials like TMDCs that present significant structural symmetry and electronic valley polarized exciton states could be adequately explored in combination with PICs to create more functionality highlights for the emerging application directions.

Next, the current deployment of 2D materials is laid on individual photonic devices. How to consolidate their role within PIC systems is an exciting topic, yet it is also full of challenges. There is excellent research that has realized light emission and photodetection within one waveguide structure[78], showing large advantages in functionalities integration and fabrication simplification. It can be expected that with the advance of three denominational monolithic heterogeneous integration and co-packaged optics technologies, 2D materials and optoelectronic devices would be integrated on-chip to form a complete scheme with high coupling efficiency and elaborate features. Light sources assisted by 2D materials generating different wavelength laser emissions, multichannel waveguides, an array of modulators, multiplexers, and 2D materials enabled broadband photodetectors, making up a WDM system to serve as building blocks for optical communication and computing. But in this mode, we may face challenges in the synergy fabrication of various 2D materials on complicated photonic circuits structures.

The last point we foresee is that wafer-scale 2D material integration with PICs will be a trend in the future. 2D materials integration promotes fabrication convenience in contrast to conventional epitaxial growth and heterogeneous integration [such as indium phosphide (InP), gallium arsenide (GaAs), Ge, and LiNbO$_3$]. By leveraging CMOS technologies, the Si-based PICs are evolving rapidly and are gradually maturing because of foundry manufacturing. Simultaneously, tremendous efforts have been taken on wafer-scale 2D materials preparation[246–249]. The following insights will be focused on combining these two fabrication flows into one industrial pilot line. It can be predicted that the integration level of 2D materials with unit cells in PICs will be dramatically promoted. However, integrating 2D materials into heterostructures and large-scale PICs remains challenging due to the difficulties in synthesizing uniform, high quality, and single crystalline materials. The cracks, wrinkles, or inhomogeneity of 2D materials when incorporated with the undulating surface of photonic architectures are also problems. Moreover, the development of packaging techniques for 2D materials within PICs is of equal importance, as many 2D

materials are sensitive to environmental factors and contamination. This ultimately impacts the working performance and reliability of PICs.

9. Conclusions

In this work, we have reviewed recent achievements in 2D materials integrated with PICs, with a focus on the four representative materials including graphene, TMDCs, BP, and hBN. Their unique properties, such as broadband absorption, ultrafast carrier mobility, strong light–matter interaction, and nonlinear effects, make them promising candidates for next-generation PICs. The ability to tune their band gaps, mechanical strength, and surface chemistry will further enhance their applicability in communications, computing sensing, and so on. Nevertheless, there are still challenges to be addressed for practical implementation, including wafer-level material preparation, reliable fabrication processes, and large-scale integration. These challenges point the way to future research endeavors. We anticipate that in the future, 2D materials will be integrated with PICs in an even more tightly-knit and scalable way, which will further promote the convergence of photonics and electronics and continually bring new opportunities for advancing photonic and optoelectronic applications.

References

1. J. D. Meindl, "Beyond Moore's law: the interconnect era," Comput. Sci. Eng. **5**, 20 (2003).
2. C. Sun, M. T. Wade, Y. Lee, J. S. Orcutt, L. Alloatti, M. S. Georgas, A. S. Waterman, J. M. Shainline, R. R. Avizienis, S. Lin, B. R. Moss, R. Kumar, F. Pavanello, A. H. Atabaki, H. M. Cook, A. J. Ou, J. C. Leu, Y.-H. Chen, K. Asanović, R. J. Ram, M. A. Popović, and V. M. Stojanović, "Single-chip microprocessor that communicates directly using light," Nature **528**, 534 (2015).
3. Y. Li, Y. Zhang, L. Zhang, and A. W. Poon, "Silicon and hybrid silicon photonic devices for intra-datacenter applications: state of the art and perspectives [Invited]," Photonics Res. **3**, B10 (2015).
4. Y. Su, Y. He, X. Guo, X. Wie, X. Ji, H. Wang, X. Cai, L. Tong, and S. Yu, "Scalability of large-scale photonic integrated circuits," ACS Photonics **10**, 2020 (2023).
5. W. N. Ye and Y. Xiong, "Review of silicon photonics: history and recent advances," J. Mod. Opt. **60**, 1299 (2013).
6. S. Mokkapati and C. Jagadish, "III-V compound SC for optoelectronic devices," Mater. Today **12**, 22 (2009).
7. P. Kharel, C. Reimer, K. Luke, L. He, and M. Zhang, "Breaking voltage–bandwidth limits in integrated lithium niobate modulators using micro-structured electrodes," Optica **8**, 357 (2021).
8. G. Chen, Y. Yu, Y. Shi, N. Li, W. Luo, L. Cao, A. J. Danner, A. Q. Liu, and X. Zhang, "High-speed photodetectors on silicon photonics platform for optical interconnect," Laser Photon. Rev. **16**, 2200117 (2022).
9. S. Lischke, A. Peczek, J. S. Morgan, K. Sun, D. Steckler, Y. Yamamoto, F. Korndörfer, C. Mai, S. Marschmeyer, M. Fraschke, A. Krüger, A. Beling, and L. Zimmermann, "Ultra-fast germanium photodiode with 3-dB bandwidth of 265 GHz," Nat. Photonics **15**, 925 (2021).
10. C. Xiang, W. Jin, D. Huang, M. A. Tran, J. Guo, Y. Wan, W. Xie, G. Kurczveil, A. M. Netherton, D. Liang, H. Rong, and J. E. Bowers, "High-performance silicon photonics using heterogeneous integration," IEEE J. Sel. Top. Quantum Electron. **28**, 8200515 (2022).
11. P. Mrowiński, P. Holewa, A. Sakanas, G. Sęk, E. Semenova, and M. Syperek, "Optimization of heterogeneously integrated InP-Si on-chip photonic components," Opt. Express **31**, 1541 (2023).

12. Z. Zhou, X. Ou, Y. Fang, E. Alkhazraji, R. Xu, Y. Wan, and J. E. Bowers, "Prospects and applications of on-chip lasers," eLight **3**, 1 (2023).

13. A. Boes, L. Chang, C. Langrock, M. Yu, M. Zhang, Q. Lin, M. Loncar, M. Fejer, J. Bowers, and A. Mitchell, "Lithium niobate photonics: unlocking the electromagnetic spectrum," Science **379**, eabj4396 (2023).

14. C. Op de Beeck, F. M. Mayor, S. Cuyvers, S. Poelman, J. F. Herrmann, O. Atalar, T. P. McKenna, B. Haq, W. Jiang, J. D. Witmer, G. Roelkens, A. H. Safavi-Naeini, R. Van Laer, and B. Kuyken, "III/V-on-lithium niobate amplifiers and lasers," Optica **8**, 1288 (2021).

15. Z. Ruan, K. Chen, Z. Wang, X. Fan, R. Gan, L. Qi, Y. Xie, C. Guo, Z. Yang, N. Cui, and L. Liu, "High-performance electro-optic modulator on silicon nitride platform with heterogeneous integration of lithium niobate," Laser Photon. Rev. **17**, 2200327 (2023).

16. C. Wang, M. Zhang, X. Chen, M. Bertrand, A. Shams-Ansari, S. Chandrasekhar, P. Winzer, and M. Loncar, "Integrated lithium niobate electro-optic modulators operating at CMOS-compatible voltages," Nature **562**, 101 (2018).

17. S. Abel, T. Stöferle, C. Marchiori, D. Caimi, L. Czornomaz, M. Stuckelberger, M. Sousa, B. J. Offrein, and J. Fompeyrine, "A hybrid barium titanate–silicon photonics platform for ultraefficient electro-optic tuning," J. Lightwave Technol. **34**, 1688 (2016).

18. A. B. Posadas, V. E. Stenger, J. DeFouw, G. Z. Mashanovich, D. Wasserman, and A. A. Demkov, "Electro-optic barium titanate modulators on silicon photonics platform," in *IEEE Silicon Photonics Conference (SiPhotonics)* (2023), p. 1.

19. M. Lee, H. E. Katz, C. Erben, D. M. Gill, P. Gopalan, J. D. Heber, and D. J. McGee, "Broadband modulation of light by using an electro-optic polymer," Science **298**, 1401 (2002).

20. D. Chen, H. R. Fetterman, A. Chen, W. H. Steier, L. R. Dalton, W. Wang, and Y. Shi, "Demonstration of 110 GHz electro-optic polymer modulators," Appl. Phys. Lett. **70**, 3335 (1997).

21. Y. Tang and K. F. Mak, "2D materials for silicon photonics," Nat. Nanotechnol. **12**, 1121 (2017).

22. D. Akinwande, C. Huyghebaert, C.-H. Wang, M. I. Serna, S. Goossens, L.-J. Li, H. S. P. Wong, and F. H. L. Koppens, "Graphene and two-dimensional materials for silicon technology," Nature **573**, 507 (2019).

23. M. H. Kryder, "Magneto-optic recording technology," J. Appl. Phys. **57**, 3913 (1985).

24. J. Wu, H. Ma, P. Yin, Y. Ge, Y. Zhang, L. Li, H. Zhang, and H. Lin, "Two-dimensional materials for integrated photonics: recent advances and future challenges," Small Sci. **1**, 2000053 (2021).

25. K. S. Novoselov, A. K. Geim, S. V. Morozov, D. Jiang, Y. Zhang, S. V. Dubonos, I. V. Grigorieva, and A. A. Firsov, "Electric field effect in atomically thin carbon films," Science **306**, 666 (2004).

26. S. Manzeli, D. Ovchinnikov, D. Pasquier, O. V. Yazyev, and A. Kis, "2D transition metal dichalcogenides," Nat. Rev. Mater. **2**, 17033 (2017).

27. A. Morita, "Semiconducting black phosphorus," Appl. Phys. A **39**, 227 (1986).

28. J. Wang, F. Ma, and M. Sun, "Graphene, hexagonal boron nitride, and their heterostructures: properties and applications," RSC Adv. **7**, 16801 (2017).

29. K. F. Mak, L. Ju, F. Wang, and T. F. Heinz, "Optical spectroscopy of graphene: from the far infrared to the ultraviolet," Solid State Commun. **152**, 1341 (2012).

30. F. Xia, H. Yan, and P. Avouris, "The interaction of light and graphene: basics, devices, and applications," Proc. IEEE **101**, 1717 (2013).

31. F. Xia, H. Wang, D. Xiao, M. Dubey, and A. Ramasubramaniam, "Two-dimensional material nanophotonics," Nat. Photonics **8**, 899 (2014).

32. K. F. Mak, C. Lee, J. Hone, J. Shan, and T. F. Heinz, "Atomically thin MoS_2: a new direct-gap semiconductor," Phys. Rev. Lett. **105**, 136805 (2010).

33. A. Splendiani, L. Sun, Y. Zhang, T. Li, J. Kim, C.-Y. Chim, G. Galli, and F. Wang, "Emerging photoluminescence in monolayer MoS_2," Nano Lett. **10**, 1271 (2010).

34. V. Tran, R. Soklaski, Y. Liang, and L. Yang, "Layer-controlled band gap and anisotropic excitons in few-layer black phosphorus," Phys. Rev. B **89**, 235319 (2014).

35. H. Liu, Y. Du, Y. Deng, and P. D. Ye, "Semiconducting black phosphorus: synthesis, transport properties and electronic applications," Chem. Soc. Rev. **44**, 2732 (2015).

36. C. R. Dean, A. F. Young, I. Meric, C. Lee, L. Wang, S. Sorgenfrei, K. Watanabe, T. Taniguchi, P. Kim, K. L. Shepard, and J. Hone, "Boron nitride substrates for high-quality graphene electronics," Nat. Nanotechnol. **5**, 722 (2010).

37. J. Dong, L. Zhang, and F. Ding, "Kinetics of graphene and 2D materials growth," Adv. Mater. **31**, 1801583 (2019).

38. X. Xu, T. Guo, H. Kim, M. K. Hota, R. S. Alsaadi, M. Lanza, X. Zhang, and H. N. Alshareef, "Growth of 2D materials at the wafer scale," Adv. Mater. **34**, 2108258 (2022).

39. Q. Zhang, D. Geng, and W. Hu, "Chemical vapor deposition for few-layer two-dimensional materials," SmartMat **4**, e1177 (2023).

40. B.-J. Park, J.-S. Choi, J.-H. Eom, H. Ha, H. Y. Kim, S. Lee, H. Shin, and S.-G. Yoon, "Defect-free graphene synthesized directly at 150°C via chemical vapor deposition with no transfer," ACS Nano **12**, 2008 (2018).

41. B. Qin, M. Z. Saeed, Q. Li, M. Zhu, Y. Feng, Z. Zhou, J. Fang, M. Hossain, Z. Zhang, Y. Zhou, Y. Huangfu, R. Song, J. Tang, B. Li, J. Liu, D. Wang, K. He, H. Zhang, R. Wu, B. Zhao, J. Li, L. Liao, Z. Wei, B. Li, X. F. Duan, and X. D. Duan, "General low-temperature growth of two-dimensional nanosheets from layered and nonlayered materials," Nat. Commun. **14**, 304 (2023).

42. Y. Gong, Z. Lin, G. Ye, G. Shi, S. Feng, Y. Lei, A. L. Elías, N. Perea-Lopez, R. Vajtai, H. Terrones, Z. Liu, M. Terrones, and P. M. Ajayan, "Tellurium-assisted low-temperature synthesis of MoS_2 and WS_2 monolayers," ACS Nano **9**, 11658 (2015).

43. H. Seok, Y. T. Megra, C. K. Kanade, J. Cho, V. K. Kanade, M. Kim, I. Lee, P. J. Yoo, H.-U. Kim, J. W. Suk, and T. Kim, "Low-temperature synthesis of wafer-scale MoS_2–WS_2 vertical heterostructures by single-step penetrative plasma sulfurization," ACS Nano **15**, 707 (2021).

44. C. Ahn, J. Lee, H.-U. Kim, H. Bark, M. Jeon, G. H. Ryu, Z. Lee, G. Y. Yeom, K. Kim, J. Jung, Y. Kim, C. Lee, and T. Kim, "Low-temperature synthesis of large-scale molybdenum disulfide thin films directly on a plastic substrate using plasma-enhanced chemical vapor deposition," Adv. Mate. **27**, 5223 (2015).

45. H. Park, T. K. Kim, S. W. Cho, H. S. Jang, S. I. Lee, and S.-Y. Choi, "Large-scale synthesis of uniform hexagonal boron nitride films by plasma-enhanced atomic layer deposition," Sci. Rep. **7**, 40091 (2017).

46. J. K. Sprenger, H. Sun, A. S. Cavanagh, A. Roshko, P. T. Blanchard, and S. M. George, "Electron-enhanced atomic layer deposition of boron nitride thin films at room temperature and 100°C," J. Phys. Chem. C **122**, 9455 (2018).

47. T. Kim, J. Mun, H. Park, D. Joung, M. Diware, C. Won, J. Park, S.-H. Jeong, and S.-W. Kang, "Wafer-scale production of highly uniform two-dimensional MoS_2 by metal-organic chemical vapor deposition," Nanotechnology **28**, 18LT01 (2017).

48. M. Romagnoli, V. Sorianello, M. Midrio, F. H. L. Koppens, C. Huyghebaert, D. Neumaier, P. Galli, W. Templ, A. D'Errico, and A. C. Ferrari, "Graphene-based integrated photonics for next-generation datacom and telecom," Nat. Rev. Mater. **3**, 392 (2018).

49. A. K. Geim, "Graphene: status and prospects," Science **324**, 1530 (2009).

50. M. J. Allen, V. C. Tung, and R. B. Kaner, "Honeycomb carbon: a review of graphene," Chem. Rev. **110**, 132 (2010).

51. P. Avouris, "Graphene: electronic and photonic properties and devices," Nano Lett. **10**, 4285 (2010).

52. G. Giovannetti, P. A. Khomyakov, G. Brocks, V. M. Karpan, J. van den Brink, and P. J. Kelly, "Doping graphene with metal contacts," Phys. Rev. Lett. **101**, 026803 (2008).

53. W. J. Yu, L. Liao, S. H. Chae, Y. H. Lee, and X. Duan, "Toward tunable band gap and tunable Dirac point in bilayer graphene with molecular doping," Nano Lett. **11**, 4759 (2011).

54. J. Yan, Y. Zhang, P. Kim, and A. Pinczuk, "Electric field effect tuning of electron-phonon coupling in graphene," Phys. Rev. Lett. **98**, 166802 (2007).

55. K. I. Bolotin, K. J. Sikes, Z. Jiang, M. Klima, G. Fudenberg, J. Hone, P. Kim, and H. L. Stormer, "Ultrahigh electron mobility in suspended graphene," Solid State Commun. **146**, 351 (2008).

56. M. Liu, X. Yin, E. Ulin-Avila, B. Geng, T. Zentgraf, L. Ju, F. Wang, and X. Zhang, "A graphene-based broadband optical modulator," Nature **474**, 64 (2011).

57. I. Meric, M. Y. Han, A. F. Young, B. Ozyilmaz, P. Kim, and K. L. Shepard, "Current saturation in zero-bandgap, top-gated graphene field-effect transistors," Nat. Nanotechnol. **3**, 654 (2008).

58. K. Chang, Z. Li, Y. Gu, K. Liu, and K. Chen, "Graphene-integrated waveguides: properties, preparation, and applications," Nano Res. **15**, 9704 (2022).

59. L. Yu, D. Dai, and S. He, "Graphene-based transparent flexible heat conductor for thermally tuning nanophotonic integrated devices," Appl. Phys. Lett. **105**, 251104 (2014).

60. L. Yu, Y. Yin, Y. Shi, D. Dai, and S. He, "Thermally tunable silicon photonic microdisk resonator with transparent graphene nanoheaters," Optica **3**, 159 (2016).

61. S. Yan, X. Zhu, L. H. Frandsen, S. Xiao, N. A. Mortensen, J. Dong, and Y. Ding, "Slow-light-enhanced energy efficiency for graphene microheaters on silicon photonic crystal waveguides," Nat. Commun. **8**, 14411 (2017).

62. S. Nakamura, K. Sekiya, S. Matano, Y. Shimura, Y. Nakade, K. Nakagawa, Y. Monnai, and H. Maki, "High-speed and on-chip optical switch based on a graphene microheater," ACS Nano **16**, 2690 (2022).

63. A. A. Balandin, S. Ghosh, W. Bao, I. Calizo, D. Teweldebrhan, F. Miao, and C. N. Lau, "Superior thermal conductivity of single-layer graphene," Nano Lett. **8**, 902 (2008).

64. Z. Fang, R. Chen, J. Zheng, A. I. Khan, K. M. Neilson, S. J. Geiger, D. M. Callahan, M. G. Moebius, A. Saxena, M. E. Chen, C. Rios, J. Hu, E. Pop, and A. Majumdar, "Ultra-low-energy programmable non-volatile silicon photonics based on phase-change materials with graphene heaters," Nat. Nanotechnol. **17**, 842 (2022).

65. Y. Hu, M. Pantouvaki, J. Van Campenhout, S. Brems, I. Asselberghs, C. Huyghebaert, P. Absil, and D. Van Thourhout, "Broadband 10 Gb/s operation of graphene electro-absorption modulator on silicon," Laser Photon. Rev. **10**, 307 (2016).

66. C. Alessandri, I. Asselberghs, S. Brems, C. Huyghebaert, J. Van Campenhout, D. Van Thourhout, and M. Pantouvaki, "High speed single-layer graphene-Si electro-absorption modulator," in CLEO Pacific Rim Conference (2018), paper Th4G.3.

67. C. Alessandri, I. Asselberghs, S. Brems, C. Huyghebaert, J. Van Campenhout, D. Van Thourhout, and M. Pantouvaki, "High speed graphene-silicon electro-absorption modulators for the O-band and C-band," Jpn J. Appl. Phys. **59**, 052008 (2020).

68. C. Alessandri, I. Asselberghs, S. Brems, C. Huyghebaert, J. Van Campenhout, D. Van Thourhout, and M. Pantouvaki, "5 × 25 Gbit/s WDM transmitters based on passivated graphene-silicon electro-absorption modulators," Appl. Opt. **59**, 1156 (2020).

69. X. Gan, R.-J. Shiue, Y. Gao, K. F. Mak, X. Yao, L. Li, A. Szep, D. Walker, Jr., J. Hone, T. F. Heinz, and D. Englund, "High-contrast electrooptic modulation of a photonic crystal nanocavity by electrical gating of graphene," Nano Lett. **13**, 691 (2013).

70. A. Majumdar, J. Kim, J. Vuckovic, and F. Wang, "Electrical control of silicon photonic crystal cavity by graphene," Nano Lett. **13**, 515 (2013).

71. M. Liu, X. Yin, and X. Zhang, "Double-layer graphene optical modulator," Nano Lett. **12**, 1482 (2012).

72. M. A. Giambra, V. Sorianello, V. Miseikis, S. Marconi, A. Montanaro, P. Galli, S. Pezzini, C. Coletti, and M. Romagnoli, "High-speed double layer graphene electro-absorption modulator on SOI waveguide," Opt. Express **27**, 20145 (2019).

73. Z. Cheng, X. Zhu, M. Galili, L. H. Frandsen, H. Hu, S. Xiao, J. Dong, Y. Ding, L. K. Oxenløwe, and X. Zhang, "Double-layer graphene on photonic crystal waveguide electro-absorption modulator with 12 GHz bandwidth," Nanophotonics **9**, 2377 (2020).

74. C. T. Phare, Y.-H. Daniel Lee, J. Cardenas, and M. Lipson, "Graphene electro-optic modulator with 30 GHz bandwidth," Nat. Photonics **9**, 511 (2015).

75. B. S. Lee, B. Kim, A. P. Freitas, A. Mohanty, Y. Zhu, G. R. Bhatt, J. Hone, and M. Lipson, "High-performance integrated graphene electro-optic modulator at cryogenic temperature," Nanophotonics **10**, 99 (2020).

76. M. Kleinert, F. Herziger, P. Reinke, C. Zawadzki, D. de Felipe, W. Brinker, H.-G. Bach, N. Keil, J. Maultzsch, and M. Schell, "Graphene-based electro-absorption modulator integrated in a passive polymer waveguide platform," Opt. Mater. Express **6**, 1800 (2016).

77. T. Lian, K. Yang, X. Wang, M. Jiang, S. Sun, D. Niu, and D. Zhang, "Electro-absorption optical modulator based on graphene-buried polymer waveguides," IEEE Photonics J. **12**, 6601610 (2020).

78. N. Youngblood, Y. Anugrah, R. Ma, S. J. Koester, and M. Li, "Multifunctional graphene optical modulator and photodetector integrated on silicon waveguides," Nano Lett. **14**, 2741 (2014).

79. M. Mohsin, D. Schall, M. Otto, A. Noculak, D. Neumaier, and H. Kurz, "Graphene based low insertion loss electro-absorption modulator on SOI waveguide," Opt. Express **22**, 15292 (2014).

80. H. Dalir, Y. Xia, Y. Wang, and X. Zhang, "Athermal broadband graphene optical modulator with 35 GHz speed," ACS Photonics **3**, 1564 (2016).

81. R. R. Nair, P. Blake, A. N. Grigorenko, K. S. Novoselov, T. J. Booth, T. Stauber, N. M. Peres, and A. K. Geim, "Fine structure constant defines visual transparency of graphene," Science **320**, 1308 (2008).

82. Y. Ding, X. Zhu, S. Xiao, H. Hu, L. H. Frandsen, N. A. Mortensen, and K. Yvind, "Effective electro-optical modulation with high extinction ratio by a graphene-silicon microring resonator," Nano Lett. **15**, 4393 (2015).

83. C. Qiu, W. Gao, R. Vajtai, P. M. Ajayan, J. Kono, and Q. Xu, "Efficient modulation of 1.55 μm radiation with gated graphene on a silicon microring resonator," Nano Lett. **14**, 6811 (2014).

84. X. Ban, M. Zhong, and B. E. Little, "Broadband hybrid plasmonic graphene modulator operating at mid-infrared wavelength," Optik **247**, 168036 (2021).

85. S. Liu, M. Wang, T. Liu, Y. Xu, J. Yue, Y. Yi, X. Sun, and D. Zhang, "Polarization-insensitive graphene modulator based on hybrid plasmonic waveguide," Photonics **9**, 609 (2022).

86. S. Liu, M. Wang, T. Liu, Y. Xu, J. Yue, Y. Yi, X. Sun, and D. Zhang, "Modulation instability of surface plasmon polaritons in graphene double-layer structure," Proc. SPIE **12569**, 125690G (2023).

87. Q. Bao and K. P. Loh, "Graphene photonics, plasmonics, and broadband optoelectronic devices," ACS Nano **6**, 3677 (2012).

88. J. Guo, J. Li, C. Liu, Y. Yin, W. Wang, Z. Ni, Z. Fu, H. Yu, Y. Xu, Y. Shi, Y. Ma, S. Gao, L. Tong, and D. Dai, "High-performance silicon-graphene hybrid plasmonic waveguide photodetectors beyond 1.55 μm," Light Sci. Appl. **9**, 29 (2020).

89. Z. Ni, L. Ma, S. Du, Y. Xu, M. Yuan, H. Fang, Z. Wang, M. Xu, D. Li, J. Yang, W. Hu, X. Pi, and D. Yang, "Plasmonic silicon quantum dots enabled high-sensitivity ultrabroadband photodetection of graphene-based hybrid phototransistors," ACS Nano **11**, 9854 (2017).

90. Z. Liang, J. Sun, Y. Jiang, L. Jiang, and X. Chen, "Plasmonic enhanced optoelectronic devices," Plasmonics **9**, 859 (2014).

91. L. Ju, B. Geng, J. Horng, C. Girit, M. Martin, Z. Hao, H. A. Bechtel, X. Liang, A. Zettl, Y. R. Shen, and F. Wang, "Graphene plasmonics for tunable terahertz metamaterials," Nat. Nanotechnol. **6**, 630 (2011).

92. S. Thongrattanasiri, F. H. L. Koppens, and F. J. García de Abajo, "Complete optical absorption in periodically patterned graphene," Phys. Rev. Lett. **108**, 047401 (2012).

93. M. H. Rezaei and M. Shiri, "High-performance tunable resonant electro-optical modulator based on suspended graphene waveguides," Opt. Express **29**, 16299 (2021).

94. R. Hao, W. Du, H. Chen, X. Jin, L. Yang, and E. Li, "Ultra-compact optical modulator by graphene induced electro-refraction effect," Appl. Phys. Lett. **103**, 061116 (2013).

95. M. Mohsin, D. Neumaier, D. Schall, M. Otto, C. Matheisen, A. L. Giesecke, A. A. Sagade, and H. Kurz, "Experimental verification of electro-refractive phase modulation in graphene," Sci. Rep. **5**, 10967 (2015).

96. V. Sorianello, M. Midrio, G. Contestabile, I. Asselberghs, J. Van Campenhout, C. Huyghebaert, I. Goykhman, A. K. Ott, A. C. Ferrari, and M. Romagnoli, "Graphene–silicon phase modulators with gigahertz bandwidth," Nat. Photonics **12**, 40 (2018).

97. V. Sorianello, G. De Angelis, T. Cassese, M. Midrio, M. Romagnoli, M. Mohsin, M. Otto, D. Neumaier, I. Asselberghs, J. Van Campenhout, and C. Huyghebaert, "Complex effective index in graphene-silicon waveguides," Opt. Express **24**, 29984 (2016).

98. H. Shu, Z. Su, L. Huang, Z. Wu, X. Wang, Z. Zhang, and Z. Zhou, "Significantly high modulation efficiency of compact graphene modulator based on silicon waveguide," Sci. Rep. **8**, 991 (2018).

99. Z. Chai, X. Hu, F. Wang, X. Niu, J. Xie, and Q. Gong, "Ultrafast all-optical switching," Adv. Opt. Mater. **5**, 1600665 (2017).

100. S. Yu, X. Wu, K. Chen, B. Chen, X. Guo, D. Dai, L. Tong, W. Liu, and Y. Ron Shen, "All-optical graphene modulator based on optical Kerr phase shift," Optica **3**, 541 (2016).

101. F. Sun, L. Xia, C. Nie, J. Shen, Y. Zou, G. Cheng, H. Wu, Y. Zhang, D. Wei, S. Yin, and C. Du, "The all-optical modulator in dielectric-loaded waveguide with graphene-silicon heterojunction structure," Nanotechnology **29**, 135201 (2018).

102. T. Guo, T. Gao, H. Zeng, L. Tang, and C. Qiu, "All-optical control of a single resonance in a graphene-on-silicon nanobeam cavity using thermo-optic effect," J. Lightwave Technol. **39**, 4710 (2021).

103. F. Sun, L. Xia, C. Nie, C. Qiu, L. Tang, J. Shen, T. Sun, L. Yu, P. Wu, S. Yin, S. Yan, and C. Du, "An all-optical modulator based on a graphene–plasmonic slot waveguide at 1550 nm," Appl. Phys. Express **12**, 042009 (2019).

104. M. Ono, M. Hata, M. Tsunekawa, K. Nozaki, H. Sumikura, H. Chiba, and M. Notomi, "Ultrafast and energy-efficient all-optical switching with graphene-loaded deep-subwavelength plasmonic waveguides," Nat. Photonics **14**, 37 (2020).

105. Z. Shi, L. Gan, T.-H. Xiao, H.-L. Guo, and Z.-Y. Li, "All-optical modulation of a graphene-cladded silicon photonic crystal cavity," ACS Photonics **2**, 1513 (2015).

106. L. Jiang, Q. Huang, and K. S. Chiang, "Low-power all-optical switch based on a graphene-buried polymer waveguide Mach–Zehnder interferometer," Opt. Express **30**, 6786 (2022).

107. T. Yu, F. Wang, Y. Xu, L. Ma, X. Pi, and D. Yang, "Graphene coupled with silicon quantum dots for high-performance bulk-silicon-based Schottky-Junction photodetectors," Adv. Mater. **28**, 4912 (2016).

108. F. Liu, K. Liu, S. Rafique, Z. Xu, W. Niu, X. Li, Y. Wang, L. Deng, J. Wang, X. Yue, T. Li, J. Wang, P. Ayala, C. Cong, Y. Qin, A. Yu, N. Chi, and Y. Zhan, "Highly efficient and stable self-powered mixed tin-lead perovskite photodetector used in remote wearable health monitoring technology," Adv. Sci. **10**, e2205879 (2023).

109. C.-H. Liu, Y.-C. Chang, T. B. Norris, and Z. Zhong, "Graphene photodetectors with ultra-broadband and high responsivity at room temperature," Nat. Nanotechnol. **9**, 273 (2014).

110. F. Xia, T. Mueller, Y.-M. Lin, A. Valdes-Garcia, and P. Avouris, "Ultrafast graphene photodetector," Nat. Nanotechnol. **4**, 839 (2009).

111. X. Gan, R.-J. Shiue, Y. Gao, I. Meric, T. F. Heinz, K. Shepard, J. Hone, S. Assefa, and D. Englund, "Chip-integrated ultrafast graphene photodetector with high responsivity," Nat. Photonics **7**, 883 (2013).

112. X. Wang, Z. Cheng, K. Xu, H. K. Tsang, and J.-B. Xu, "High-responsivity graphene/silicon-heterostructure waveguide photodetectors," Nat. Photonics **7**, 888 (2013).

113. A. Pospischil, M. Humer, M. M. Furchi, D. Bachmann, R. Guider, T. Fromherz, and T. Mueller, "CMOS-compatible graphene photodetector covering all optical communication bands," Nat. Photonics **7**, 892 (2013).

114. D. Schall, D. Neumaier, M. Mohsin, B. Chmielak, J. Bolten, C. Porschatis, A. Prinzen, C. Matheisen, W. Kuebart, B. Junginger, W. Templ, A. L. Giesecke, and H. Kurz, "50 Gbit/s photodetectors based on wafer-scale graphene for integrated silicon photonic communication systems," ACS Photonics **1**, 781 (2014).

115. H. Jiang, J. Wei, F. Sun, C. Nie, C. Fu, H. Shi, J. Sun, X. Wei, and C. W. Qiu, "Enhanced photogating effect in graphene photodetectors via potential fluctuation engineering," ACS Nano **16**, 4458 (2022).

116. J. C. Song, M. S. Rudner, C. M. Marcus, and L. S. Levitov, "Hot carrier transport and photocurrent response in graphene," Nano Lett. **11**, 4688 (2011).

117. S. Piscanec, M. Lazzeri, F. Mauri, A. C. Ferrari, and J. Robertson, "Kohn anomalies and electron-phonon interactions in graphite," Phys. Rev. Lett. **93**, 185503 (2004).

118. R. Bistritzer and A. H. MacDonald, "Electronic cooling in graphene," Phys. Rev. Lett. **102**, 206410 (2009).

119. D. Sun, G. Aivazian, A. M. Jones, J. S. Ross, W. Yao, D. Cobden, and X. Xu, "Ultrafast hot-carrier-dominated photocurrent in graphene," Nat. Nanotechnol. **7**, 114 (2012).

120. K. J. Tielrooij, L. Piatkowski, M. Massicotte, A. Woessner, Q. Ma, Y. Lee, K. S. Myhro, C. N. Lau, P. Jarillo-Herrero, N. F. van Hulst, and F. H. Koppens, "Generation of photovoltage in graphene on a femtosecond timescale through efficient carrier heating," Nat. Nanotechnol. **10**, 437 (2015).

121. S. Schuler, D. Schall, D. Neumaier, L. Dobusch, O. Bethge, B. Schwarz, M. Krall, and T. Mueller, "Controlled generation of a p-n junction in a waveguide integrated graphene photodetector," Nano Lett. **16**, 7107 (2016).

122. S. Schuler, J. E. Muench, A. Ruocco, O. Balci, D. V. Thourhout, V. Sorianello, M. Romagnoli, K. Watanabe, T. Taniguchi, I. Goykhman, A. C. Ferrari, and T. Mueller, "High-responsivity graphene photodetectors integrated on silicon microring resonators," Nat. Commun. **12**, 3733 (2021).

123. M. Freitag, T. Low, F. Xia, and P. Avouris, "Photoconductivity of biased graphene," Nat. Photonics **7**, 53 (2013).

124. J. Gosciniak and J. B. Khurgin, "On-chip ultrafast plasmonic graphene hot electron bolometric photodetector," ACS Omega **5**, 14711 (2020).

125. J. Yan, M. H. Kim, J. A. Elle, A. B. Sushkov, G. S. Jenkins, H. M. Milchberg, M. S. Fuhrer, and H. D. Drew, "Dual-gated bilayer graphene hot-electron bolometer," Nat. Nanotechnol. **7**, 472 (2012).

126. J. Gosciniak, M. Rasras, and J. B. Khurgin, "Ultrafast plasmonic graphene photodetector based on the channel photothermoelectric effect," ACS Photonics **7**, 488 (2020).

127. J. E. Muench, A. Ruocco, M. A. Giambra, V. Miseikis, D. Zhang, J. Wang, H. F. Y. Watson, G. C. Park, S. Akhavan, V. Sorianello, A. Midrio, A. Tomadin, C. Coletti, M. Romagnoli, A. C. Ferrari, and I. Goykhman, "Waveguide-integrated, plasmonic enhanced graphene photodetectors," Nano Lett. **19**, 7632 (2019).

128. Z. Ma, K. Kikunaga, H. Wang, S. Sun, R. Amin, R. Maiti, M. H. Tahersima, H. Dalir, M. Miscuglio, and V. J. Sorger, "Compact graphene plasmonic slot photodetector on silicon-on-insulator with high responsivity," ACS Photonics **7**, 932 (2020).

129. V. Ryzhii, M. Ryzhii, D. S. Ponomarev, V. G. Leiman, V. Mitin, M. S. Shur, and T. Otsuji, "Negative photoconductivity and hot-carrier bolometric detection of terahertz radiation in graphene-phosphorene hybrid structures," J. Appl. Phys. **125**, 151608 (2019).

130. N. Youngblood, C. Chen, S. J. Koester, and M. Li, "Waveguide-integrated black phosphorus photodetector with high responsivity and low dark current," Nat. Photonics **9**, 247 (2015).

131. R.-J. Shiue, Y. Gao, Y. Wang, C. Peng, A. D. Robertson, D. K. Efetov, S. Assefa, F. H. Koppens, J. Hone, and D. Englund, "High-responsivity graphene-boron nitride photodetector and autocorrelator in a silicon photonic integrated circuit," Nano Lett. **15**, 7288 (2015).

132. S. Yan, Y. Zuo, S. Xiao, L. K. Oxenløwe, and Y. Ding, "Graphene photodetector employing double slot structure with enhanced responsivity and large bandwidth," Opto-Electronic Advances **5**, 210159 (2022).

133. I. Vangelidis, D. V. Bellas, S. Suckow, G. Dabos, S. Castilla, F. H. L. Koppens, A. C. Ferrari, N. Pleros, and E. Lidorikis, "Unbiased plasmonic-assisted integrated graphene photodetectors," ACS Photonics **9**, 1992 (2022).

134. P. Ma, Y. Salamin, B. Baeuerle, A. Josten, W. Heni, A. Emboras, and J. Leuthold, "Plasmonically enhanced graphene photodetector featuring 100 Gbit/s data reception, high responsivity, and compact size," ACS Photonics **6**, 154 (2018).

135. M. A. Giambra, V. Mišeikis, S. Pezzini, S. Marconi, A. Montanaro, F. Fabbri, V. Sorianello, A. C. Ferrari, C. Coletti, and M. Romagnoli, "Wafer-scale integration of graphene-based photonic devices," ACS Nano **15**, 3171 (2021).

136. H. Guan, J. Hong, X. Wang, J. Ming, Z. Zhang, A. Liang, X. Han, J. Dong, W. Qiu, Z. Chen, H. Lu, and H. Zhang, "Broadband, high-sensitivity graphene photodetector based on ferroelectric polarization of lithium niobate," Adv. Opt. Mater. **9**, 2100245 (2021).

137. S. Zhu, Y. Zhang, Y. Ren, Y. Wang, K. Zhai, H. Feng, Y. Jin, Z. Lin, J. Feng, S. Li, Q. Yang, N. H. Zhu, E. Y.-B. Pun, and C. Wang, "Waveguide-integrated two-dimensional material photodetectors in thin-film lithium niobate," Adv. Photonics Res. **4**, 2300045 (2023).

138. C. Wu, S. Brems, D. Yudistira, D. Cott, A. Milenin, K. Vandersmissen, A. Maestre, A. Centeno, A. Zurutuza, J. Van Campenhout, C. Huyghebaert, D. Van Thourhout, and M. Pantouvaki, "Wafer-scale integration of single layer graphene electro-absorption modulators in a 300 mm CMOS pilot line," Laser Photon. Rev. **17**, 2200789 (2023).

139. N. Huo, Y. Yang, and J. Li, "Optoelectronics based on 2D TMDs and heterostructures," J. Semicond. **38**, 031002 (2017).

140. C. Tan and H. Zhang, "Two-dimensional transition metal dichalcogenide nanosheet-based composites," Chem. Soc. Rev. **44**, 2713 (2015).

141. Q. H. Wang, K. Kalantar-Zadeh, A. Kis, J. N. Coleman, and M. S. Strano, "Electronics and optoelectronics of two-dimensional transition metal dichalcogenides," Nat. Nanotechnol. **7**, 699 (2012).

142. M. M. Ugeda, A. J. Bradley, S. F. Shi, F. H. da Jornada, Y. Zhang, D. Y. Qiu, W. Ruan, S. K. Mo, Z. Hussain, Z. X. Shen, F. Wang, S. G. Louie, and M. F. Crommie, "Giant bandgap renormalization and excitonic effects in a monolayer transition metal dichalcogenide semiconductor," Nat. Mater. **13**, 1091 (2014).

143. A. Ramasubramaniam, "Large excitonic effects in monolayers of molybdenum and tungsten dichalcogenides," Phys. Rev. B **86**, 115409 (2012).

144. H. J. Kim, G. H. Ahn, J. Cho, M. Amani, J. P. Mastandrea, C. K. Groschner, D. H. Lien, Y. Zhao, J. W. Ager, III, M. C. Scott, D. C. Chrzan, and A. Javey,

"Synthetic WSe$_2$ monolayers with high photoluminescence quantum yield," Sci. Adv. **5**, eaau4728 (2019).

145. H. Chen, V. Corboliou, A. S. Solntsev, D. Y. Choi, M. A. Vincenti, D. de Ceglia, C. de Angelis, Y. Lu, and D. N. Neshev, "Enhanced second-harmonic generation from two-dimensional MoSe$_2$ on a silicon waveguide," Light Sci. Appl. **6**, e17060 (2017).

146. N. Kumar, S. Najmaei, Q. Cui, F. Ceballos, P. M. Ajayan, J. Lou, and H. Zhao, "Second harmonic microscopy of monolayer MoS$_2$," Phys. Rev. B **87**, 161403(R) (2013).

147. X. Wen, Z. Gong, and D. Li, "Nonlinear optics of two-dimensional transition metal dichalcogenides," InfoMat **1**, 317 (2019).

148. S. Wu, S. Buckley, J. R. Schaibley, L. Feng, J. Yan, D. G. Mandrus, F. Hatami, W. Yao, J. Vučković, A. Majumdar, and X. Xu, "Monolayer semiconductor nanocavity lasers with ultralow thresholds," Nature **520**, 69 (2015).

149. X. Ge, M. Minkov, S. Fan, X. Li, and W. Zhou, "Laterally confined photonic crystal surface emitting laser incorporating monolayer tungsten disulfide," NPJ 2D Mater. Appl. **3**, 16 (2019).

150. Y. Ye, Z. J. Wong, X. Lu, X. Ni, H. Zhu, X. Chen, Y. Wang, and X. Zhang, "Monolayer excitonic laser," Nat. Photonics **9**, 733 (2015).

151. O. Salehzadeh, M. Djavid, N. H. Tran, I. Shih, and Z. Mi, "Optically pumped two-dimensional MoS$_2$ lasers operating at room-temperature," Nano Lett. **15**, 5302 (2015).

152. J. C. Reed, A. Y. Zhu, H. Zhu, F. Yi, and E. Cubukcu, "Wavelength tunable microdisk cavity light source with a chemically enhanced MoS$_2$ emitter," Nano Lett. **15**, 1967 (2015).

153. N. M. H. Duong, Z.-Q. Xu, M. Kianinia, R. Su, Z. Liu, S. Kim, C. Bradac, T. T. Tran, Y. Wan, L.-J. Li, A. Solntsev, J. Liu, and I. Aharonovich, "Enhanced emission from WSe$_2$ monolayers coupled to circular Bragg gratings," ACS Photonics **5**, 3950 (2018).

154. J. Sung, D. Shin, H. Cho, S. W. Lee, S. Park, Y. D. Kim, J. S. Moon, J.-H. Kim, and S.-H. Gong, "Room-temperature continuous-wave indirect-bandgap transition lasing in an ultra-thin WS$_2$ disk," Nat. Photonics **16**, 792 (2022).

155. Y.-Q. Bie, G. Grosso, M. Heuck, M. M. Furchi, Y. Cao, J. Zheng, D. Bunandar, E. Navarro-Moratalla, L. Zhou, D. K. Efetov, T. Taniguchi, K. Watanabe, J. Kong, D. Englund, and P. Jarillo-Herrero, "A MoTe$_2$-based light-emitting diode and photodetector for silicon photonic integrated circuits," Nat. Nanotechnol. **12**, 1124 (2017).

156. Y. Li, J. Zhang, D. Huang, H. Sun, F. Fan, J. Feng, Z. Wang, and C. Z. Ning, "Room-temperature continuous-wave lasing from monolayer molybdenum ditelluride integrated with a silicon nanobeam cavity," Nat. Nanotechnol. **12**, 987 (2017).

157. H. Fang, J. Liu, H. Li, L. Zhou, L. Liu, J. Li, X. Wang, T. F. Krauss, and Y. Wang, "1305 nm few-layer MoTe$_2$-on-silicon laser-like emission," Laser Photon. Rev. **12**, 1800015 (2018).

158. E. Y. Paik, L. Zhang, G. W. Burg, R. Gogna, E. Tutuc, and H. Deng, "Interlayer exciton laser of extended spatial coherence in atomically thin heterostructures," Nature **576**, 80 (2019).

159. Y. Liu, H. Fang, A. Rasmita, Y. Zhou, J. Li, T. Yu, Q. Xiong, N. Zheludev, J. Liu, and W. Gao, "Room temperature nanocavity laser with interlayer excitons in 2D heterostructures," Sci. Adv. **5**, eaav4506 (2019).

160. R. Maiti, C. Patil, M. A. S. R. Saadi, T. Xie, J. G. Azadani, B. Uluutku, R. Amin, A. F. Briggs, M. Miscuglio, D. Van Thourhout, S. D. Solares, T. Low, R. Agarwal, S. R. Bank, and V. J. Sorger, "Strain-engineered high-responsivity MoTe$_2$ photodetector for silicon photonic integrated circuits," Nat. Photonics **14**, 578 (2020).

161. X. Zong, H. Hu, G. Ouyang, J. Wang, R. Shi, L. Zhang, Q. Zeng, C. Zhu, S. Chen, C. Cheng, B. Wang, H. Zhang, Z. Liu, W. Huang, T. Wang, L. Wang, and X. Chen, "Black phosphorus-based van der Waals heterostructures for mid-infrared light-emission applications," Light Sci. Appl. **9**, 114 (2020).

162. O. Lopez-Sanchez, D. Lembke, M. Kayci, A. Radenovic, and A. Kis, "Ultrasensitive photodetectors based on monolayer MoS$_2$," Nat. Nanotechnol. **8**, 497 (2013).

163. J. Wu, H. Schmidt, K. K. Amara, X. Xu, G. Eda, and B. Ozyilmaz, "Large thermoelectricity via variable range hopping in chemical vapor deposition grown single-layer MoS$_2$," Nano Lett. **14**, 2730 (2014).

164. W. Zhang, M. H. Chiu, C. H. Chen, W. Chen, L. J. Li, and A. T. Wee, "Role of metal contacts in high-performance phototransistors based on WSe$_2$ monolayers," ACS Nano **8**, 8653 (2014).

165. P. Ma, N. Flöry, Y. Salamin, B. Baeuerle, A. Emboras, A. Josten, T. Taniguchi, K. Watanabe, L. Novotny, and J. Leuthold, "Fast MoTe$_2$ waveguide photodetector with high sensitivity at telecommunication wavelengths," ACS Photonics **5**, 1846 (2018).

166. N. Flöry, P. Ma, Y. Salamin, A. Emboras, T. Taniguchi, K. Watanabe, J. Leuthold, and L. Novotny, "Waveguide-integrated van der Waals heterostructure photodetector at telecom wavelengths with high speed and high responsivity," Nat. Nanotechnol. **15**, 118 (2020).

167. Y. Gao, G. Zhou, H. K. Tsang, and C. Shu, "High-speed van der Waals heterostructure tunneling photodiodes integrated on silicon nitride waveguides," Optica **6**, 514 (2019).

168. X. X. Liang, H. Guan, K. Luo, Z. He, A. Liang, W. Zhang, Q. Lin, Z. Yang, H. Zhang, C. Xu, H. Xie, F. Liu, F. Ma, T. Yang, and H. Lu, "Van der Waals integrated LiNbO$_3$/WS$_2$ for high-performance UV–Vis–NIR photodetection," Laser Photon. Rev. 2300286 (2023).

169. J. F. Gonzalez Marin, D. Unuchek, K. Watanabe, T. Taniguchi, and A. Kis, "MoS$_2$ photodetectors integrated with photonic circuits," npj 2D Mater. Appl. **3**, 14 (2019).

170. Y. Yi, Z. Sun, J. Li, P. K. Chu, and X. F. Yu, "Optical and optoelectronic properties of black phosphorus and recent photonic and optoelectronic applications," Small Methods **3**, 1900165 (2019).

171. Y. Xu, Z. Shi, X. Shi, K. Zhang, and H. Zhang, "Recent progress in black phosphorus and black-phosphorus-analogue materials: properties, synthesis and applications," Nanoscale **11**, 14491 (2019).

172. Y. Cai, G. Zhang, and Y.-W. Zhang, "Layer-dependent band alignment and work function of few-layer phosphorene," Sci. Rep. **4**, 6677 (2014).

173. S. Das, W. Zhang, M. Demarteau, A. Hoffmann, M. Dubey, and A. Roelofs, "Tunable transport gap in phosphorene," Nano Lett. **14**, 5733 (2014).

174. B. Deng, V. Tran, Y. Xie, H. Jiang, C. Li, Q. Guo, X. Wang, H. Tian, S. J. Koester, H. Wang, J. J. Cha, Q. Xia, L. Yang, and F. Xia, "Efficient electrical control of thin-film black phosphorus bandgap," Nat. Commun. **8**, 14474 (2017).

175. C. R. Ryder, J. D. Wood, S. A. Wells, and M. C. Hersam, "Chemically tailoring semiconducting two-dimensional transition metal dichalcogenides and black phosphorus," ACS Nano **10**, 3900 (2016).

176. J. Kim, S. S. Baik, S. H. Ryu, Y. Sohn, S. Park, B. G. Park, J. Denlinger, Y. Yi, H. J. Choi, and K. S. Kim, "Observation of tunable band gap and anisotropic Dirac semimetal state in black phosphorus," Science **349**, 723 (2015).

177. A. S. Rodin, A. Carvalho, and A. H. Castro Neto, "Strain-induced gap modification in black phosphorus," Phys. Rev. Lett. **112**, 176801 (2014).

178. H. Kim, S. Z. Uddin, D. H. Lien, M. Yeh, N. S. Azar, S. Balendhran, T. Kim, N. Gupta, J. Rho, C. P. Grigoropoulos, K. B. Crozier, and A. Javey, "Actively variable-spectrum optoelectronics with black phosphorus," Nature **596**, 232 (2021).

179. L. Li, Y. Yu, G. J. Ye, Q. Ge, X. Ou, H. Wu, D. Feng, X. H. Chen, and Y. Zhang, "Black phosphorus field-effect transistors," Nat. Nanotechnol. **9**, 372 (2014).

180. S. Zhang, J. Yang, R. Xu, F. Wang, W. Li, M. Ghufran, Y. W. Zhang, Z. Yu, G. Zhang, Q. Qin, and Y. Lu, "Extraordinary photoluminescence and strong temperature/angle-dependent Raman responses in few-layer phosphorene," ACS Nano **8**, 9590 (2014).

181. L. Li, J. Kim, C. Jin, G. J. Ye, D. Y. Qiu, F. H. da Jornada, Z. Shi, L. Chen, Z. Zhang, F. Yang, K. Watanabe, T. Taniguchi, W. Ren, S. G. Louie, X. H. Chen, Y. Zhang, and F. Wang, "Direct observation of the layer-dependent electronic structure in phosphorene," Nat. Nanotechnol. **12**, 21 (2017).

182. J. Zheng, Z. Yang, C. Si, Z. Liang, X. Chen, R. Cao, Z. Guo, K. Wang, Y. Zhang, J. Ji, M. Zhang, D. Fan, and H. Zhang, "Black phosphorus based all-optical-signal-processing: toward high performances and enhanced stability," ACS Photonics **4**, 1466 (2017).

183. K. Wang, B. M. Szydlowska, G. Wang, X. Zhang, J. J. Wang, J. J. Magan, L. Zhang, J. N. Coleman, J. Wang, and W. J. Blau, "Ultrafast nonlinear excitation dynamics of black phosphorus nanosheets from visible to mid-infrared," ACS Nano **10**, 6923 (2016).

184. S. Huang and X. Ling, "Black phosphorus: optical characterization, properties and applications," Small **13**, 1700823 (2017).

185. C. Chen, N. Youngblood, R. Peng, D. Yoo, D. A. Mohr, T. W. Johnson, S. H. Oh, and M. Li, "Three-dimensional integration of black phosphorus photodetector with silicon photonics and nanoplasmonics," Nano Lett. **17**, 985 (2017).

186. Y. Yin, R. Cao, J. Guo, C. Liu, J. Li, X. Feng, H. Wang, W. Du, A. Qadir, H. Zhang, Y. Ma, S. Gao, Y. Xu, Y. Shi, L. Tong, and D. Dai, "High-speed and high-responsivity hybrid silicon/black-phosphorus waveguide photodetectors at 2 μm," Laser Photon. Rev. **13**, 1900032 (2019).

187. S. Yuan, D. Naveh, K. Watanabe, T. Taniguchi, and F. Xia, "A wavelength-scale black phosphorus spectrometer," Nat. Photonics **15**, 601 (2021).

188. Y. Ma, B. Dong, J. Wei, Y. Chang, L. Huang, K. W. Ang, and C. Lee, "High-responsivity mid-infrared black phosphorus slow light waveguide photodetector," Adv. Opt. Mater. **8**, 2000337 (2020).

189. R. Tian, L. Gu, Y. Ji, C. Li, Y. Chen, S. Hu, Z. Li, X. Gan, and J. Zhao, "Black phosphorus photodetector enhanced by a planar photonic crystal cavity," ACS Photonics **8**, 3104 (2021).

190. Y. Xue, X. Wu, K. Chen, J. Wang, and L. Liu, "Waveguide integrated high-speed black phosphorus photodetector on a thin-film lithium niobate platform," Opt. Mater. Express **13**, 272 (2023).

191. S. N. S. Yadav, P.-L. Chen, C. H. Liu, and T. J. Yen, "Plasmonic metasurface integrated black phosphorus-based mid-infrared photodetector with high responsivity and speed," Adv. Mater. Interfaces **10**, 2202403 (2023).

192. S. Wang, R. J. Chapman, B. C. Johnson, I. Krasnokutska, J. L. J. Tambasco, K. Messalea, A. Peruzzo, and J. Bullock, "Integration of black phosphorus photoconductors with lithium niobate on insulator photonics," Adv. Opt. Mater. **11**, 2201688 (2023).

193. Q. Cai, D. Scullion, W. Gan, A. Falin, S. Zhang, K. Watanabe, T. Taniguchi, Y. Chen, E. J. G. Santos, and L. H. Li, "High thermal conductivity of high-quality monolayer boron nitride and its thermal expansion," Sci. Adv. **5**, eaav0129 (2019).

194. C. Elias, P. Valvin, T. Pelini, A. Summerfield, C. J. Mellor, T. S. Cheng, L. Eaves, C. T. Foxon, P. H. Beton, S. V. Novikov, B. Gil, and G. Cassabois, "Direct band-gap crossover in epitaxial monolayer boron nitride," Nat. Commun. **10**, 2639 (2019).

195. L. Liu, Y. P. Feng, and Z. X. Shen, "Structural and electronic properties of h-BN," Phys. Rev. B **68**, 104102 (2003).

196. M. Yankowitz, Q. Ma, P. Jarillo-Herrero, and B. J. LeRoy, "Van der Waals heterostructures combining graphene and hexagonal boron nitride," Nat. Rev. Phys. **1**, 112 (2019).

197. Z. Liu, L. Ma, G. Shi, W. Zhou, Y. Gong, S. Lei, X. Yang, J. Zhang, J. Yu, K. P. Hackenberg, A. Babakhani, J. C. Idrobo, R. Vajtai, J. Lou, and P. M. Ajayan, "In-plane heterostructures of graphene and hexagonal boron nitride with controlled domain sizes," Nat. Nanotechnol. **8**, 119 (2013).

198. J. D. Caldwell, I. Aharonovich, G. Cassabois, J. H. Edgar, B. Gil, and D. N. Basov, "Photonics with hexagonal boron nitride," Nat. Rev. Mater. **4**, 552 (2019).

199. J. Ren and P. Innocenzi, "2D boron nitride heterostructures: recent advances and future challenges," Small Struct. **2**, 2100068 (2021).

200. Q. Li, M. Liu, Y. Zhang, and Z. Liu, "Hexagonal boron nitride-graphene heterostructures: synthesis and interfacial properties," Small **12**, 32 (2016).

201. D. N. Futaba, "Hexagonal boron nitride heterostructures go large," Nat. Electron. **6**, 104 (2023).

202. T. Q. P. Vuong, G. Cassabois, P. Valvin, E. Rousseau, A. Summerfield, C. J. Mellor, Y. Cho, T. S. Cheng, J. D. Albar, L. Eaves, C. T. Foxon, P. H. Beton, S. V. Novikov, and B. Gil, "Deep ultraviolet emission in hexagonal boron nitride grown by high-temperature molecular beam epitaxy," 2D Mater. **4**, 021023 (2017).

203. D. V. Shtansky, K. L. Firestein, and D. V. Golberg, "Fabrication and application of BN nanoparticles, nanosheets and their nanohybrids," Nanoscale **10**, 17477 (2018).

204. S. Kim, N. M. H. Duong, M. Nguyen, T. J. Lu, M. Kianinia, N. Mendelson, A. Solntsev, C. Bradac, D. R. Englund, and I. Aharonovich, "Integrated on chip platform with quantum emitters in layered materials," Adv. Opt. Mater. **7**, 1901132 (2019).

205. Y. Liu, N. O. Weiss, X. Duan, H.-C. Cheng, Y. Huang, and X. Duan, "Van der Waals heterostructures and devices," Nat. Rev. Mater. **1**, 16042 (2016).

206. A. K. Geim and I. V. Grigorieva, "Van der Waals heterostructures," Nature **499**, 419 (2013).

207. D. Jariwala, T. J. Marks, and M. C. Hersam, "Mixed-dimensional van der Waals heterostructures," Nat. Mater. **16**, 170 (2017).

208. J.-S. Kim and J. T. Kim, "Silicon electro-absorption modulator based on graphene-hexagonal boron nitride heterostructure," J. Lightwave Technol. **34**, 5293 (2016).

209. H. Agarwal, B. Terres, L. Orsini, A. Montanaro, V. Sorianello, M. Pantouvaki, K. Watanabe, T. Taniguchi, D. V. Thourhout, M. Romagnoli, and F. H. L. Koppens, "2D-3D integration of hexagonal boron nitride and a high-k dielectric for ultrafast graphene-based electro-absorption modulators," Nat. Commun. **12**, 1070 (2021).

210. A. Kuzmina, M. Parzefall, P. Back, T. Taniguchi, K. Watanabe, A. Jain, and L. Novotny, "Resonant light emission from graphene/hexagonal boron nitride/graphene tunnel junctions," Nano Lett. **21**, 8332 (2021).

211. X. Hong, J. Kim, S. F. Shi, Y. Zhang, C. Jin, Y. Sun, S. Tongay, J. Wu, Y. Zhang, and F. Wang, "Ultrafast charge transfer in atomically thin MoS_2/WS_2 heterostructures," Nat. Nanotechnol. **9**, 682 (2014).

212. M. S. Choi, B. K. Cheong, C. H. Ra, S. Lee, J. H. Bae, S. Lee, G. D. Lee, C. W. Yang, J. Hone, and W. J. Yoo, "Electrically driven reversible phase changes in layered In_2Se_3 crystalline film," Adv. Mater. **29**, 1703568 (2017).

213. T. Li, Y. Wang, W. Li, D. Mao, C. J. Benmore, I. Evangelista, H. Xing, Q. Li, F. Wang, G. Sivaraman, A. Janotti, S. Law, and T. Gu, "Structural phase transitions between layered indium selenide for integrated photonic memory," Adv. Mater. **34**, 2108261 (2022).

214. P. Li, Y. Chen, T. Yang, Z. Wang, H. Lin, Y. Xu, L. Li, H. Mu, B. N. Shivananju, Y. Zhang, Q. Zhang, A. Pan, S. Li, D. Tang, B. Jia, H. Zhang, and Q. Bao, "Two-dimensional $CH_3NH_3PbI_3$ perovskite nanosheets for ultrafast pulsed fiber lasers," ACS Appl. Mater. Interfaces **9**, 12759 (2017).

215. H. Lu, Y. Liu, P. Ahlawat, A. Mishra, W. R. Tress, F. T. Eickemeyer, Y. Yang, F. Fu, Z. Wang, C. E. Avalos, B. I. Carlsen, A. Agarwalla, X. Zhang, X. Li, Y. Zhan, S. M. Zakeeruddin, L. Emsley, U. Rothlisberger, L. Zheng, A. Hagfeldt, and M. Gratzel, "Vapor-assisted deposition of highly efficient, stable black-phase $FAPbI_3$ perovskite solar cells," Science **370**, eabb8985 (2020).

216. P. J. Cegielski, A. L. Giesecke, S. Neutzner, C. Porschatis, M. Gandini, D. Schall, C. A. R. Perini, J. Bolten, S. Suckow, S. Kataria, B. Chmielak, T. Wahlbrink, A. Petrozza, and M. C. Lemme, "Monolithically integrated perovskite semiconductor lasers on silicon photonic chips by scalable top-down fabrication," Nano Lett. **18**, 6915 (2018).

217. A. Ren, H. Wang, L. Dai, J. Xia, X. Bai, E. Butler-Caddle, J. A. Smith, H. Lai, J. Ye, X. Li, S. Zhan, C. Yao, Z. Li, M. Tang, X. Liu, J. Bi, B. Li, S. Kai, R. Chen, H. Yan, J. Hong, L. Yuan, I. P. Marko, A. Wonfor, F. Fu, S. A. Hindmarsh, A. M. Sanchez, J. Lloyd-Hughes, S. J. Sweeney, A. Rao, N. C. Greenham, J. Wu, Y. Li, Q. Cheng, R. H. Friend, R. V. Penty, I. H. White, H. J. Snaith, and W. Zhang, "High-bandwidth perovskite photonic sources on silicon," Nat. Photonics **17**, 798 (2023).

218. H. Kim, Z. Wang, and H. N. Alshareef, "MXetronics: electronic and photonic applications of MXenes," Nano Energy **60**, 179 (2019).

219. J. Li, C. Wang, B. Zhang, Z. Wang, W. Yu, Y. Chen, X. Liu, Z. Guo, and H. Zhang, "Artificial carbon graphdiyne: status and challenges in nonlinear photonic and optoelectronic applications," ACS Appl. Mater. Interfaces **12**, 49281 (2020).

220. Y. Zhao, P. Guo, X. Li, and Z. Jin, "Ultrafast photonics application of graphdiyne in the optical communication region," Carbon **149**, 336 (2019).

221. Y. Yao, X. Xia, Z. Cheng, K. Wei, X. Jiang, J. Dong, and H. Zhang, "All-optical modulator using MXene inkjet-printed microring resonator," IEEE J. Sel. Top. Quantum Electron. **26**, 5900306 (2020).

222. A. Hazan, B. Ratzker, D. Zhang, A. Katiyi, M. Sokol, Y. Gogotsi, and A. Karabchevsky, "MXene-nanoflakes-enabled all-optical nonlinear activation function for on-chip photonic deep neural networks," Adv. Mater. **35**, 2210216 (2023).

223. Y. Huang, Y.-H. Pan, R. Yang, L. H. Bao, L. Meng, H. L. Luo, Y. Q. Cai, G. D. Liu, W. J. Zhao, Z. Zhou, L. M. Wu, Z. L. Zhu, M. Huang, L. W. Liu, L. Liu, P. Cheng, K. H. Wu, S. B. Tian, C. Z. Gu, Y. G. Shi, Y. F. Guo, Z. G. Cheng, J. P. Hu, L. Zhao, G. H. Yang, E. Sutter, P. Sutter, Y. L. Wang, W. Ji, X. J. Zhou, and H. J. Gao, "Universal mechanical exfoliation of large-area 2D crystals," Nat. Commun. **11**, 2453 (2020).

224. E. Gao, S.-Z. Lin, Z. Qin, M. J. Buehler, X.-Q. Feng, and Z. Xu, "Mechanical exfoliation of two-dimensional materials," J. Mech. Phys. Solids **115**, 248 (2018).

225. J.-Y. Moon, M. Kim, S.-I. Kim, S. Xu, J. H. Choi, D. Whang, K. Watanabe, T. Taniguchi, D. S. Park, J. Seo, S. H. Cho, S. K. Son, and J. H. Lee, "Layer-engineered large-area exfoliation of graphene," Sci. Adv. **6**, eabc6601 (2020).

226. J. Shim, S.-H. Bae, W. Kong, D. Lee, K. Qiao, D. Nezich, Y. J. Park, R. Zhao, S. Sundaram, X. Li, H. Yeon, C. Choi, H. Kum, R. Yue, G. Zhou, Y. Ou, K. Lee, J. Moodera, X. Zhao, J. H. Ahn, C. Hinkle, A. Ougazzaden, and J. Kim, "Controlled crack propagation for atomic precision handling of wafer-scale two-dimensional materials," Science **362**, 665 (2018).

227. F. Liu, W. Wu, Y. Bai, S. H. Chae, Q. Li, J. Wang, J. Hone, and X. Y. Zhu, "Disassembling 2D van der Waals crystals into macroscopic monolayers and reassembling into artificial lattices," Science **367**, 903 (2020).

228. V. Nicolosi, M. Chhowalla, M. G. Kanatzidis, M. S. Strano, and J. N. Coleman, "Liquid exfoliation of layered materials," Science **340**, 1226419 (2013).

229. J. N. Coleman, M. Lotya, A. O'Neill, S. D. Bergin, P. J. King, U. Khan, K. Young, A. Gaucher, S. De, R. J. Smith, I. V. Shvets, S. K. Arora, G. Stanton, H. Y. Kim, K. Lee, G. T. Kim, G. S. Duesberg, T. Hallam, J. J. Boland, J. J. Wang, J. F. Donegan, J. C. Grunlan, G. Moriarty, A. Shmeliov, R. J. Nicholls, J. M. Perkins, E. M. Grieveson, K. Theuwissen, D. W. McComb, P. D. Nellist, and V. Nicolosi, "Two-dimensional nanosheets produced by liquid exfoliation of layered materials," Science **331**, 568 (2011).

230. C. Huo, Z. Yan, X. Song, and H. Zeng, "2D materials via liquid exfoliation: a review on fabrication and applications," Sci. Bull. **60**, 1994 (2015).

231. F. Withers, H. Yang, L. Britnell, A. P. Rooney, E. Lewis, A. Felten, C. R. Woods, V. Sanchez Romaguera, T. Georgiou, A. Eckmann, Y. J. Kim, S. G. Yeates, S. J. Haigh, A. K. Geim, K. S. Novoselov, and C. Casiraghi, "Heterostructures produced from nanosheet-based inks," Nano Lett. **14**, 3987 (2014).

232. A. G. Kelly, D. Finn, A. Harvey, T. Hallam, and J. N. Coleman, "All-printed capacitors from graphene-BN-graphene nanosheet heterostructures," Appl. Phys. Lett. **109**, 023107 (2016).

233. T. Carey, S. Cacovich, G. Divitini, J. Ren, A. Mansouri, J. M. Kim, C. Wang, C. Ducati, R. Sordan, and F. Torrisi, "Fully inkjet-printed two-dimensional material field-effect heterojunctions for wearable and textile electronics," Nat. Commun. **8**, 1202 (2017).

234. X. Jiang, W. Li, T. Hai, R. Yue, Z. Chen, C. Lao, Y. Ge, G. Xie, Q. Wen, and H. Zhang, "Inkjet-printed MXene micro-scale devices for integrated broadband ultrafast photonics," npj 2D Mater. Appl. **3**, 34 (2019).

235. T. H. Ly, M.-H. Chiu, M.-Y. Li, J. Zhao, D. J. Perello, M. O. Cichocka, H. M. Oh, S. H. Chae, H. Y. Jeong, F. Yao, L. J. Li, and Y. H. Lee, "Observing grain boundaries in CVD-grown monolayer transition metal dichalcogenides," ACS Nano **8**, 11401 (2014).

236. A. T. Hoang, K. Qu, X. Chen, and J. H. Ahn, "Large-area synthesis of transition metal dichalcogenides via CVD and solution-based approaches and their device applications," Nanoscale **13**, 615 (2021).

237. A. Bansal, M. Hilse, B. Huet, K. Wang, A. Kozhakhmetov, J. H. Kim, S. Bachu, N. Alem, R. Collazo, J. A. Robinson, R. Engel-Herbert, and J. M. Redwing, "Substrate modification during chemical vapor deposition of hBN on sapphire," ACS Appl. Mater. Interfaces **13**, 54516 (2021).

238. K. Zhang, Y. Feng, F. Wang, Z. Yang, and J. Wang, "Two dimensional hexagonal boron nitride (2D-hBN): synthesis, properties and applications," J. Mater. Chem. C Mater. **5**, 11992 (2017).

239. K. Chen, X. Zhou, X. Cheng, R. Qiao, Y. Cheng, C. Liu, Y. Xie, W. Yu, F. Yao, Z. Sun, F. Wang, K. Liu, and Z. Liu, "Graphene photonic crystal fibre with strong and tunable light–matter interaction," Nat. Photonics **13**, 754 (2019).

240. Q. Wu, W. Wongwiriyapan, J.-H. Park, S. Park, S. J. Jung, T. Jeong, S. Lee, Y. H. Lee, and Y. J. Song, "*In situ* chemical vapor deposition of graphene and hexagonal boron nitride heterostructures," Curr. Appl. Phys. **16**, 1175 (2016).

241. Z. Shi, R. Yang, L. Zhang, Y. Wang, D. Liu, D. Shi, E. Wang, and G. Zhang, "Patterning graphene with zigzag edges by self-aligned anisotropic etching," Adv. Mater. **23**, 3061 (2011).

242. J. Song, F.-Y. Kam, R.-Q. Png, W. L. Seah, J. M. Zhuo, G. K. Lim, P. K. Ho, and L. L. Chua, "A general method for transferring graphene onto soft surfaces," Nat. Nanotechnol. **8**, 356 (2013).

243. L. Dong, H. Al-Mumen, F. Rao, and W. Li, "Singular sheet etching of graphene with oxygen plasma," Nanomicro Lett. **6**, 116 (2014).

244. J. Wu, H. Li, Z. Yin, H. Li, J. Liu, X. Cao, Q. Zhang, and H. Zhang, "Layer thinning and etching of mechanically exfoliated MoS$_2$ nanosheets by thermal annealing in air," Small **9**, 3314 (2013).

245. N. Clark, L. Nguyen, M. J. Hamer, F. Schedin, E. A. Lewis, E. Prestat, A. Garner, Y. Cao, M. Zhu, R. Kashtiban, J. Sloan, D. Kepaptsoglou, R. V. Gorbachev, and S. J. Haigh, "Scalable patterning of encapsulated black phosphorus," Nano Lett. **18**, 5373 (2018).

246. Z. Wu, Y. Lyu, Y. Zhang, R. Ding, B. Zheng, Z. Yang, S. P. Lau, X. H. Chen, and J. Hao, "Large-scale growth of few-layer two-dimensional black phosphorus," Nat. Mater. **20**, 1203 (2021).

247. X. Gao, L. Zheng, F. Luo, J. Qian, J. Wang, M. Yan, W. Wang, Q. Wu, J. Tang, Y. Cao, C. Tan, J. Tang, M. Zhu, Y. Wang, Y. Li, L. Sun, G. Gao, J. Yin, L. Lin, Z. Liu, S. Qin, and H. Peng, "Integrated wafer-scale ultra-flat graphene by gradient surface energy modulation," Nat. Commun. **13**, 5410 (2022).

248. X. Li, J. Yang, H. Sun, L. Huang, H. Li, and J. Shi, "Controlled synthesis and accurate doping of wafer-scale two-dimensional semiconducting transition metal dichalcogenides," Adv. Mater. 2305115 (2023).

249. S. Fukamachi, P. Solís-Fernández, K. Kawahara, D. Tanaka, T. Otake, Y.-C. Lin, K. Suenaga, and H. Ago, "Large-area synthesis and transfer of multilayer hexagonal boron nitride for enhanced graphene device arrays," Nat. Electron. **6**, 126 (2023).

250. H. Tan, Z. Ni, W. Peng, S. Du, X. Liu, S. Zhao, W. Li, Z. Ye, M. Xu, Y. Xu, X. Pi, and D. Yang, "Broadband optoelectronic synaptic devices based on silicon nanocrystals for neuromorphic computing," Nano Energy **52**, 422 (2018).

251. Z. He, H. Guan, X. Liang, J. Chen, X. Mie, K. Luo, R. An, L. Ma, F. Ma, T. Yang, and H. Lu, "Broadband, polarization-sensitive, and self-powered high-performance photodetection of hetero-integrated MoS$_2$ on lithium niobate," Research **6**, 0199 (2023).